The Astrophysical Journal, 983:29 (28pp), 2025 April 10 https://doi.org/10.3847/1538-4357/adb620

Eight Years of Light from ASASSN-15oi: Toward Understanding the Late-time Evolution of TDEs

A. Hajela[1], K. D. Alexander[2], R. Margutti[3,4], R. Chornock[3], M. Bietenholz[5], C. T. Christy[2], M. Stroh[6], G. Terreran[7,8], R. Saxton[9], S. Komossa[10], J. S. Bright[3,11], E. Ramirez-Ruiz[12], D. L. Coppejans[13], J. K. Leung[14,15,16], Y. Cendes[17], E. Wiston[3], T. Laskar[18,19], A. Horesh[16], G. Schroeder[6,20], Nayana A. J.[3], M. H. Wieringa[21], N. Velez[17], E. Berger[22], P. K. Blanchard[6], T. Eftekhari[6,20], S. Gomez[23], M. Nicholl[24], H. Sears[25], and B. A. Zauderer[26]

[1] DARK, Niels Bohr Institute, University of Copenhagen, Jagtvej 155, 2200 Copenhagen, Denmark; aprajita.hajela@gmail.com
[2] Department of Astronomy and Steward Observatory, University of Arizona, 933 North Cherry Avenue, Tucson, AZ 85721-0065, USA
[3] Department of Astronomy, University of California, Berkeley, CA 94720-3411, USA
[4] Department of Physics, University of California, Berkeley, CA 94720-7300, USA
[5] SARAO/Hartebeesthoek Radio Astronomy Observatory, PO Box 443, Krugersdorp, 1740, South Africa
[6] Center for Interdisciplinary Exploration and Research in Astrophysics (CIERA), Northwestern University, Evanston, IL 60208, USA
[7] Las Cumbres Observatory, 6740 Cortona Drive, Suite 102, Goleta, CA 93117-5575, USA
[8] Department of Physics, University of California, Santa Barbara, CA 93106-9530, USA
[9] Telespazio UK for ESA, ESAC, Apartado 78, 28691 Villanueva de la Cañada, Madrid, Spain
[10] Max-Planck Institut für Radioastronomie, Auf dem Hügel 69, 53121 Bonn, Germany
[11] Astrophysics, Department of Physics, University of Oxford, Keble Road, Oxford OX1 3RH, UK
[12] Department of Astronomy and Astrophysics, University of California, Santa Cruz, CA 95064, USA
[13] Department of Physics, University of Warwick, Gibbet Hill Road, CV4 7AL Coventry, UK
[14] David A. Dunlap Department of Astronomy and Astrophysics, University of Toronto, 50 St. George Street, Toronto, ON M5S 3H4, Canada
[15] Dunlap Institute for Astronomy and Astrophysics, University of Toronto, 50 St. George Street, Toronto, ON M5S 3H4, Canada
[16] Racah Institute of Physics, The Hebrew University of Jerusalem, Jerusalem 91904, Israel
[17] Department of Physics, University of Oregon, Eugene, OR 97403, USA
[18] Department of Physics & Astronomy, University of Utah, Salt Lake City, UT 84112, USA
[19] Department of Astrophysics/IMAPP, Radboud University, P.O. Box 9010, 6500 GL, Nijmegen, The Netherlands
[20] Department of Physics and Astronomy, Northwestern University, 2145 Sheridan Road, Evanston, IL 60208-3112, USA
[21] CSIRO Space and Astronomy, Australia Telescope National Facility, PO Box 76, 1710, Epping, NSW, Australia
[22] Center for Astrophysics | Harvard & Smithsonian, Cambridge, MA 02138, USA
[23] Space Telescope Science Institute, 3700 San Martin Drive, Baltimore, MD 21218, USA
[24] Astrophysics Research Centre, School of Mathematics and Physics, Queens University Belfast, Belfast BT7 1NN, UK
[25] Department of Physics and Astronomy, Rutgers, The State University of New Jersey, 136 Frelinghuysen Road, Piscataway, NJ 08854-8019, USA
[26] National Science Foundation, 2415 Eisenhower Avenue, Alexandria, VA 22314, USA

Received 2024 July 26; revised 2025 January 17; accepted 2025 February 12; published 2025 April 2

Abstract

We present results from an extensive follow-up campaign of the tidal disruption event (TDE) ASASSN-15oi spanning $\delta t \sim$ 10–3000 days, offering an unprecedented window into the multiwavelength properties of a TDE during its first $\approx$8 yr of evolution. ASASSN-15oi is one of the few TDEs with strong detections at X-ray, optical/UV, and radio wavelengths and it also featured two delayed radio flares at $\delta t \sim 180$ days and $\delta t \sim 1400$ days. Our observations at $\delta t > 1400$ days reveal an absence of thermal X-rays, a late-time variability in the nonthermal X-ray emission, and sharp declines in the nonthermal X-ray and radio emission at $\delta t \sim 2800$ days and $\sim$3000 days, respectively. The UV emission shows no significant evolution at $\delta t > 400$ days and remains above the pre-TDE level. We show that a cooling envelope model can explain the thermal emission consistently across all epochs. We also find that a scenario involving episodic ejection of material due to stream–stream collisions can possibly explain the first radio flare. Given the peculiar spectral and temporal evolution of the late-time emission, however, constraining the origins of the second radio flare and the nonthermal X-rays remains challenging. Our study underscores the critical role of long-term, multiwavelength follow-up to fully characterize the extended evolutionary phases of a TDE.

Unified Astronomy Thesaurus concepts: Tidal disruption (1696); Accretion (14); Radio transient sources (2008); Ultraviolet transient sources (1854); X-ray transient sources (1852)

1. Introduction

When a star straying too close to a supermassive black hole (SMBH) of mass $\lesssim 10^8\,M_\odot$ in the center of a galaxy is torn apart by the strong tidal forces of the black hole, an energetic and short-lived transient event known as a tidal disruption event (TDE) is triggered (J. G. Hills 1975; M. J. Rees 1988; C. R. Evans & C. S. Kochanek 1989; J. Guillochon & E. Ramirez-Ruiz 2013). Through emitting radiation across the electromagnetic spectrum, TDEs provide an exclusive window to study previously dormant SMBHs, accretion physics on human-accessible timescales, initiation and cessation of the launched outflows, and the makeup of the nuclear environment of the host galaxies (e.g., C. Bonnerot & N. C. Stone 2021; J. L. Dai et al. 2021; S. Gezari 2021). Early TDE data sets typically had limited temporal and spectral coverage, but as the quality and quantity of data have improved, observations have uncovered a broad diversity at every wavelength of the electromagnetic spectrum. In this context, the TDE ASASSN-15oi stands out for its uniquely detailed data set, with X-ray, optical, UV, and radio detections spanning $\sim$3000 days. We briefly review the current landscape of TDE observations before focusing on ASASSN-15oi as a valuable test case of TDE emission models.

The first TDE candidates were discovered as X-ray transients, but more TDEs are now identified via wide-sky optical surveys. Reviews of X-ray discovered TDEs can be found in S. Komossa (2002), K. Auchettl et al. (2017), R. Saxton et al. (2021) and S. Komossa & D. Grupe (2023), while M. Guolo et al. (2024) and E. Hammerstein et al. (2023) discussed X-ray properties of optically discovered TDEs. "Soft" X-rays, characterized by a power-law (PL) spectrum with photon index $\Gamma_X > 3$ or a blackbody (BB) spectrum with temperature $kT_{\rm BB} \sim 0.05$ keV, emerge from regions at distances of $\sim 10^{11}$–10^{12} cm from the SMBH. These distances are consistent with r_g, the gravitational radii around $\sim 10^6$–$10^7\,M_\odot$ nonrotating SMBHs, implying that soft X-rays are emitted from the material actively accreting onto the SMBH (L. Dai et al. 2018). "Hard" X-rays ($\Gamma_X \lesssim 2$ power law) can result either from synchrotron radiation or by Compton up-scattering of thermal disk photons by electrons in a corona or in an outflow. TDEs detected in X-rays show either, both, or neither of these components. ASASSN-15oi is one of the few TDEs to show both a "hard" and "soft" X-ray component (this work; see also S. Gezari et al. 2017; T. W. S. Holoien et al. 2018).

The physical origin of the optical and UV emission in TDEs is less certain. This emission arises at radii $\sim 10^{15}$ cm $\gg r_g$. One potential scenario involves the reprocessing of disk X-rays by material at these extended radii (J. Guillochon et al. 2014; N. Roth et al. 2016; L. Dai et al. 2018; L. L. Thomsen et al. 2022). Such material could be disk winds (e.g., M. C. Miller 2015), or outflows launched during the circularization process (B. D. Metzger & N. C. Stone 2016) or during stream–stream collisions (also known as collision-induced outflows, CIOs, in W. Lu & C. Bonnerot 2020). This scenario predicts that the post-optical-peak luminosity should trace the mass fallback rate with a characteristic temporal decay of $t^{-5/3}$, as indeed observed in many TDEs (e.g., B. Mockler et al. 2019; S. Gezari 2021). Another scenario, as proposed by T. Piran et al. (2015), is where the optical luminosity is powered directly by the stream–stream collisions, with the gravitationally bound stellar debris stream returning to the SMBH and self-intersecting. Recently, a third scenario (inspired by A. Loeb & A. Ulmer 1997) was revived and reanalyzed by B. D. Metzger (2022), where the optical emission results from the radiative cooling of a quasi-spherical, pressure-supported envelope formed as a result of the stellar disruption. This *cooling envelope* model predicts the optical/UV luminosity to decline as $t^{-3/2}$, coincidentally resembling the $t^{-5/3}$ decay from the reprocessing scenario.

Radio emission from TDEs is primarily powered by synchrotron radiation from outflows interacting with the surrounding medium at larger distances ($\gtrsim 10^{16}$ cm) from the SMBH (K. D. Alexander et al. 2020 and references therein). While most radio detected TDEs show evidence for non-relativistic outflows, such as in ASASSN-14li (K. D. Alexander et al. 2016; J. Krolik et al. 2016; but also see S. van Velzen et al. 2016 for an alternate scenario involving a weak jet), only $\sim$1% of the TDEs show evidence for powerful on-axis relativistic jets, like Swift J1644+57 (e.g., J. S. Bloom et al. 2011; D. N. Burrows et al. 2011; A. J. Levan et al. 2011; B. A. Zauderer et al. 2011; E. Berger et al. 2012; T. Eftekhari et al. 2018; Y. Cendes et al. 2021b). Notably, not all TDEs are detected in radio, and early campaigns often ceased observations if sources remained undetected or faded below the sensitivity limits of the telescopes (M. M. Anderson et al. 2020).

However, owing to systematic long-term monitoring campaigns, recent studies have revealed that a large fraction of TDEs ($\sim$40%) exhibit significant radio emission of ~months to years after discovery (A. Anumarlapudi et al. 2024; Y. Cendes et al. 2024). Some examples include iPTF16fnl (A. Horesh et al. 2021b), AT 2018hyz (Y. Cendes et al. 2022; I. Sfaradi et al. 2024), and IGR J12580+0134 (E. S. Perlman et al. 2022). Among this subset, ASASSN-15oi was the first TDE to show multiple flares (A. Horesh et al. 2021a): a late-time radio brightening at $\delta t \sim 180$ days, and a second brightening[27] about 3.5 yr later, as seen in the VLA Sky Survey (VLASS) data. Our team independently identified this bright radio source in VLASS data, and began a multiwavelength follow-up campaign that covers the time period $\delta t = 1471$–2970 days, on which we report here.

ASASSN-15oi was discovered in optical on 2015 August 14 (J. Brimacombe et al. 2015) at a luminosity distance of $\sim$216 Mpc (T. W. S. Holoien et al. 2016; S. Gezari et al. 2017) by the All-Sky Automated Survey for SuperNovae (ASAS-SN; B. Shappee et al. 2014). In this paper, we measure δt as the time elapsed since discovery. Observations of ASASSN-15oi at optical, UV, and X-ray wavelengths at $\delta t \lesssim 600$ days were previously reported in T. W. S. Holoien et al. (2016, 2018), S. Gezari et al. (2017), and J. T. Hinkle et al. (2021). In addition to its peculiar radio behavior, ASASSN-15oi also belongs to the rare class of He-TDEs (P. Charalampopoulos et al. 2022), that are characterized by broad He II emission lines in their spectra. It is also one of the only three known iron rich TDEs[28] with Fe II lines identified in its $\delta t = 330$ days spectrum (T. Wevers et al. 2019). The optical and UV luminosity initially showed an exponential decay at $\delta t < 100$ days. The optical emission subsequently faded to the level of the host galaxy at $\gtrsim$300 days (T. W. S. Holoien et al. 2016, 2018; S. Gezari et al. 2017) while the emission at UV wavelengths remained above the pre-TDE host galaxy level.

The X-ray emission from ASASSN-15oi was initially weaker ($\sim 10^{42}$ erg s^{-1}) compared to other X-ray bright TDEs in the literature ($\sim 10^{43}$ erg s^{-1}; M. Guolo et al. 2024), but it later brightened by a factor of $\sim$6 between $\delta t \approx 80$ and $\approx$230 days. Previous studies identified two contributing components to the X-ray emission: a blackbody component responsible for the delayed brightening of the X-ray emission; and a power-law component reported as remaining nearly

---

[27] Some TDEs with early radio emission have also shown delayed rebrightenings: AT 2019azh rebrightened at $\sim$200 days (I. Sfaradi et al. 2022), similar to the time of the first radio flare detection in ASASSN-15oi, but unlike ASASSN-15oi, it showed prompt radio emission starting just 21 days post-discovery. AT 2020vwl rebrightened after $\sim$1000 days (A. J. Goodwin et al. 2025), similar to the time of the second radio flare of ASASSN-15oi. The radio emission modeling of AT 2020vwl in A. J. Goodwin et al. (2023), however, also suggests a prompt outflow launch.

[28] Other iron rich TDEs are AT 2018fyk (T. Wevers et al. 2021) and AT 2019dsg (G. Cannizzaro et al. 2021). PS16dtm and PS1-10adi also exhibit Fe II lines; however, both of them are TDE events in an already existing active galactic nucleus (AGN).

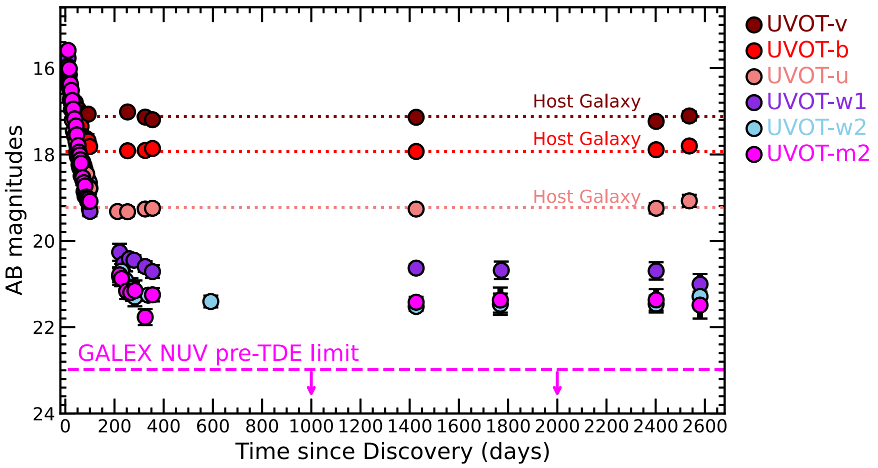

Figure 1. Long-term evolution of ASASSN-15oi as captured by Swift-UVOT. Filled circles mark the total emission (i.e., TDE + host galaxy) at the location of ASASSN-15oi. While at $\delta t \gtrsim 300$ days the optical emission is dominated by the host galaxy light (horizontal dotted lines as determined by J. T. Hinkle et al. 2021), the UV emission at the location of ASASSN-15oi remains bright and does not relax to the pre-TDE UV flux levels (horizontal dashed line). Magnitudes have been corrected for Galactic extinction.

constant, leading to its association with a preexisting active galactic nucleus (AGN; S. Gezari et al. 2017). We note that the archival mid-infrared colors of ASASSN-15oi's host galaxy, with W1 − W2 ~ 0.06, from the Wide-field Infrared Survey Explorer (E. L. Wright et al. 2010), are inconsistent with the presence of any strong AGN activity (R. J. Assef et al. 2013, 2018), as was also reported in T. W. S. Holoien et al. (2018).

Our aim in this study is to investigate the emission from ASASSN-15oi using the complete multiwavelength data set spanning 8 yr since its discovery. Our data set includes previously published data ($\delta t \lesssim 600$ days), other publicly available observations ($\delta t \gtrsim 600$ days), as well as new observations that we acquired after the onset of the second radio flare at $\delta t = 1471$–2970 days. We reanalyze the previously reported observations in a manner consistent with that used for our new ones, and report our inferences on the origin of the emission from ASASSN-15oi across its various evolutionary stages. The paper is organized as follows: in Section 2, we outline the details of the multiwavelength observations and our data reduction. In Section 3, we fit the radio spectral energy distributions (SEDs) with different models under the umbrella assumption that the radio observations are powered by synchrotron emission. In Section 4 we divide the emission from ASASSN-15oi into thermal and nonthermal components, discuss the possible origins of the emission at different wavelengths, and investigate any potential intercorrelations. We provide a summary and conclusions in Section 5.

2. Observations and Data Analysis

In this Section, we present new data spanning the time period $\delta t \approx 600$–3000 days, acquired by a variety of telescopes: Swift-UVOT, Swift-XRT,[29] X-ray Multi-MirrorMission (XMM-Newton), Karl G. Jansky Very Large Array (VLA), Very Long Baseline Array (VLBA), Australia Telescope Compact Array (ATCA), MeerKAT telescope, and the Atacama Large Millimeter/submillimeter Array (ALMA). Furthermore to perform a systematic analysis, we homogeneously reduce all of the observations over the time period of $\delta t = 8$–3000 days.

2.1. UV: Swift-UVOT

Swift-UVOT (N. Gehrels et al. 2004; P. W. A. Roming et al. 2005) observed ASASSN-15oi from 2015 August 23 until 2022 October 19 ($\delta t = 8$–2580 days). We analyzed all available Swift-UVOT photometric data following the prescriptions of P. J. Brown et al. (2009), with the updated calibration files (T. S. Poole et al. 2008; A. A. Breeveld et al. 2010). All photometry was extracted using a 5″ radius aperture and a region of 36″ radius free of sources for the background. When possible, we merged observations to achieve a minimum source detection significance of $\approx 10\sigma$. Finally, we corrected for Galactic extinction assuming the E. L. Fitzpatrick (1999) reddening law and $R_V = 3.1$.[30] The resulting extinction corrections are $A_v = 0.185$ mag, $A_b = 0.245$ mag, $A_u = 0.294$ mag, $A_{w1} = 0.377$ mag, $A_{w2} = 0.551$ mag, and $A_{m2} = 0.547$ mag. The Swift-UVOT photometry is presented in Table A1 and the long-term UV evolution of ASASSN-15oi is shown in Figure 1. For observations at $\delta t < 500$ days, we find excellent agreement with the photometry presented in J. T. Hinkle et al. (2021). We use the UV/optical bolometric luminosities (for epochs where optical emission was above the host galaxy level) from J. T. Hinkle et al. (2021) for our analysis.

In stark contrast to the X-ray and radio emission that show dramatic temporal variability on short timescales (Sections 2.2, 2.3, 2.4), the late-time Swift-UVOT photometry at $\delta t > 600$ days is consistent with constant flux (Figure 1), showing no significant evidence for fading at $\delta t \approx 500$–2600 days in any of the Swift-UVOT filters. However, at these epochs, at optical wavelengths (i.e., Swift-UVOT *u*, *b*, and *v* filters), the flux is consistent with the pre-TDE host galaxy level as determined by the updated host galaxy modeling of J. T. Hinkle et al. (2021). However, at UV wavelengths (i.e., Swift-UVOT uvw1, uvw2, and uvm2 filters), we confirm the presence of an excess of emission that was reported by T. W. S. Holoien et al. (2018)

---

[29] For Swift data, we provide a self-consistent flux calibration of the entire data set that accounts for the spectral evolution of the source.

[30] J. T. Hinkle et al. (2021) adopted a J. A. Cardelli et al. (1989) reddening law. Here we adopted the E. L. Fitzpatrick (1999) reddening law following the findings of E. F. Schlafly & D. P. Finkbeiner (2011). For the $R_V = 3.1$ curves, the difference in the A_λ values of Swift-UVOT filters is $\leqslant 0.015$ mag.

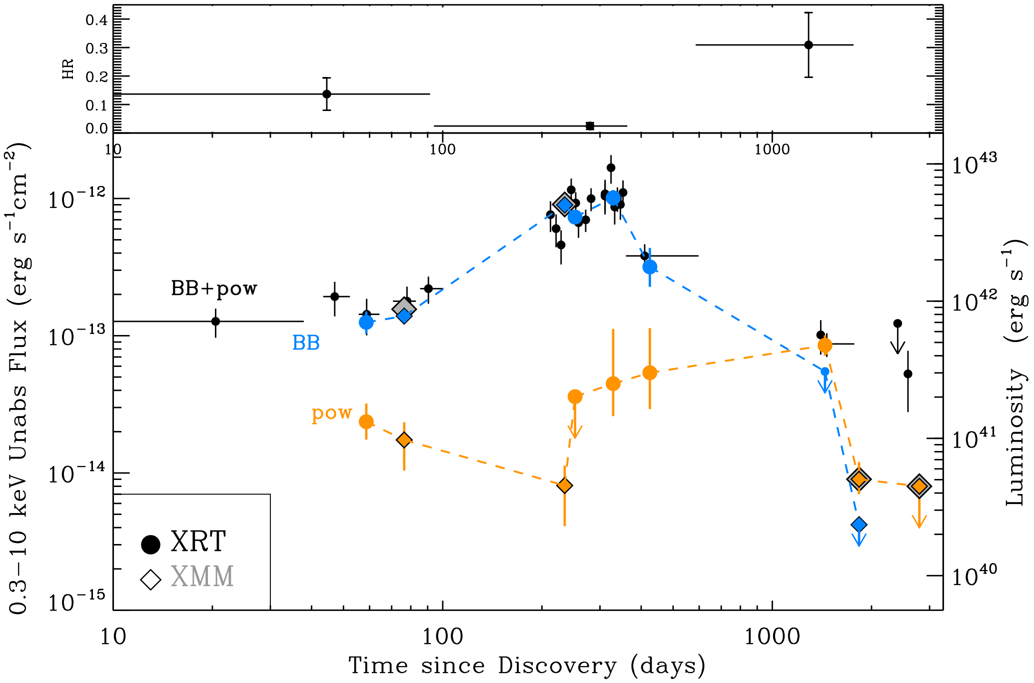

Figure 2. Long-term evolution of ASASSN-15oi as captured by Swift-XRT (circles) and XMM-Newton (diamonds) in 0.3–10 keV. The data have been corrected for Galactic absorption. The rise of the X-ray emission at $\delta t \leqslant 350$ days is dominated by a blackbody component (blue), while a power-law spectral component (orange) dominates the emission at $\delta t \geqslant 1400$ days. At >1400 days, the thermal X-rays become nondetectable and the nonthermal X-rays show variability, showing a sharp decline in the latest observation at $\delta t = 2794$ days. The count-to-flux factors obtained from the time-resolved spectral analysis of ASASSN-15oi with the seven XRT spectra are interpolated in time to convert the individual XRT count-rates to total unabsorbed fluxes and luminosities (plotted in black circles here; see details in Section 2.2). The total XMM unabsorbed fluxes and luminosities are plotted with gray diamonds. The spectra of the two most recent XRT observations and the latest XMM observation cannot be fitted with the complex two-component model; therefore, the corresponding flux and luminosity are computed using a power-law-only fit. Top panel: temporal evolution of the hardness ratio (HR). HR is defined as the ratio of the Swift-XRT counts in 1.5–10 keV to the counts in 0.3–1.5 keV. The very soft emission around the time of the light-curve peak is followed by hardening as the blackbody component subsides.

using data at earlier epochs (at $\delta t \approx$ 250–600 days). As of $\delta t = 2600$ days, with $m_{w1} \approx 21$ mag, $m_{w2} \approx 22$ mag and $m_{m2} \approx 22$ mag (observed mags, AB system), ASASSN-15oi is ≈0.7 mag, ≈1.5 mag and ≈0.9 mag brighter, respectively, than the best-fitting pre-TDE host galaxy model of J. T. Hinkle et al. (2021). From a completely observational perspective that is independent from the host galaxy light modeling, pre-TDE Galaxy Evolution Explorer (GALEX) observations constrain the UV emission of the host galaxy to be $m_{\rm NUV} > 22.98$ mag (T. W. S. Holoien et al. 2018; J. T. Hinkle et al. 2021). For the blackbody spectrum with $T \sim 2 \times 10^4$ K that best fits the late-time UVOT data, the GALEX NUV to Swift-UVOT *uvm*2 filter correction term is δmag ≈ 0.05 mag, which implies that at $\delta t \approx 2600$ days, the UV emission is $\gtrsim$2.3 times brighter than in the pre-TDE era. Similarly persistent UV excesses of emission have been found in ASASSN-14li (G. C. Brown et al. 2017), as well as in other TDEs (S. van Velzen et al. 2019; A. Mummery et al. 2024). We note that since optical discovery, ASASSN-15oi has radiated $\sim 1.2 \times 10^{51}$ erg at UV and optical wavelengths. Finally, we note the presence of an unrelated optical/UV source (S1 hereafter) at ≈10″ from ASASSN-15oi.

2.2. X-Rays: Swift-XRT

We analyzed Swift-XRT data (N. Gehrels et al. 2004; D. N. Burrows et al. 2005) using online tools[31] (P. A. Evans et al. 2009) and custom `IDL` scripts following the prescriptions in R. Margutti et al. (2013). Swift-XRT observed ASASSN-15oi starting on 2015 August 23 ($\delta t = 8$ days). Observations acquired under IDs 00033999 and 00095141 extend to 2020 June 21 ($\delta t = 1773$ days). They show a progressive brightening of the source until $\delta t \approx 350$ days, followed by rapid fading by a factor ∼10 in luminosity by $\delta t \approx 600$ days, as can be seen in Figure 2 (see also Figure 3 from S. Gezari et al. 2017 and Figure 6 from T. W. S. Holoien et al. 2018). Additional XRT observations of ASASSN-15oi acquired between ≈ 1400–1460 days show fainter but persistent X-ray emission. A later epoch of Swift-XRT data was acquired on 2022 March 11 ($\delta t = 2401$ days) under ID 00096018. No X-ray source was detected at the location of the transient, and we infer a 3σ upper limit on the count-rate of $4.3 \times 10^{-3}\,{\rm c\,s^{-1}}$ (exposure time of 7.2 ks, 0.3–10 keV). Finally, ASASSN-15oi was observed with Swift-XRT between 2022 July and October (δt = 2536–2623 days). We found marginal evidence (at the level of $\approx 3.5\sigma$, Gaussian equivalent) for X-ray emission at the location of ASASSN-15oi with count-rate $(1.3 \pm 0.6) \times 10^{-3}\,{\rm c\,s^{-1}}$ (exposure time of 7.0 ks, 0.3–10 keV).

We extracted seven spectra (Table A2) by grouping observations close in time. Following T. W. S. Holoien et al. (2016, 2018) and S. Gezari et al. (2017), we fitted the spectra in the 0.3–10 keV energy range with an absorbed two-component model featuring a (nonthermal) power law and a (thermal) blackbody, i.e., `tbabs*(cflux*pow+cflux*bbody)` within `XSPEC` v12.12.1. The Galactic neutral hydrogen column density in the direction of the transient is $N_{\rm H,gal} = 5.6 \times 10^{20}\,{\rm cm^{-2}}$ (P. M. W. Kalberla et al. 2005). We found no evidence for intrinsic absorption, and we thus assume $N_{\rm H,int} = 0\,{\rm cm^{-2}}$. The

---

[31] The Swift-XRT data products generator, https://www.swift.ac.uk/user_objects/docs.php.

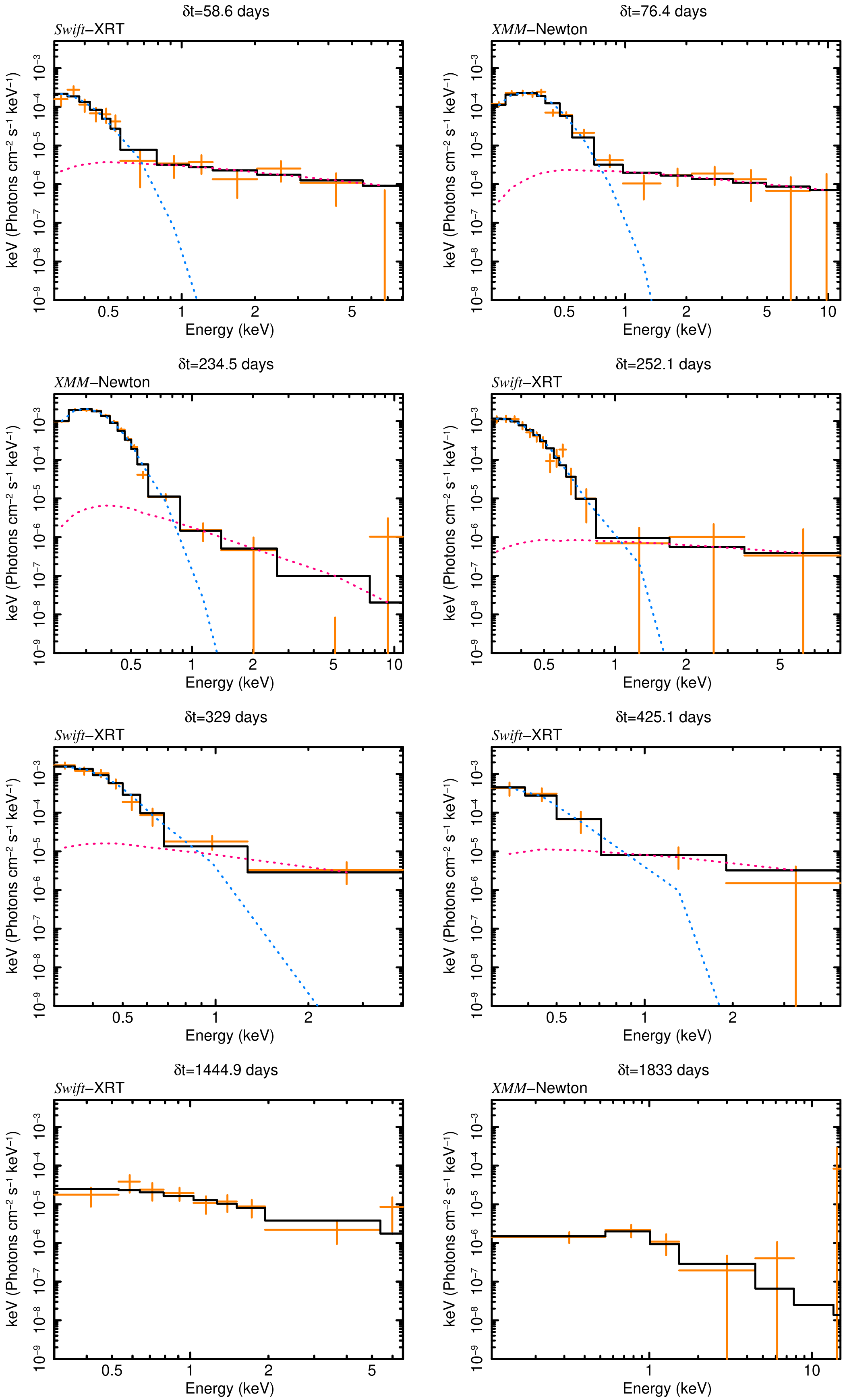

Figure 3. Unfolded X-ray spectra of ASASSN-15oi ranging from $\delta t \approx 76.4$ days to 1833 days in the 0.2–12 (0.3–10) keV energy range as observed by XMM-Newton (Swift-XRT). We plot spectra here where we have a high signal-to-noise ratio (S/N). Blue (pink) dashed line: blackbody (power-law) component. For all of the plots, the *y*-axis covers the same dynamical range. At late times, the blackbody component that was responsible for the source brightening until $\delta t \approx 350$ days becomes undetectable and the spectrum consists of an absorbed simple power law.

temporal evolution of the relative flux of the thermal and nonthermal spectral components in ASASSN-15oi implies a time-varying count-to-flux conversion factor. Following R. Margutti et al. (2013), we used the results from the time-resolved spectral analysis to perform a self-consistent flux calibration of the count-rate light curve. Specifically, we calculated a count-to-flux conversion as a function of time since discovery by linearly interpolating in the log space the count-to-flux conversion factors derived from the seven spectra. For each of the seven spectra, the best-fitting blackbody temperature ($kT_{\rm BB}$), blackbody radius $R_{\rm BB}$, power-law index $\Gamma_{\rm X}$, unabsorbed fluxes corresponding to respective components, and total absorbed fluxes are reported in Table A2. The X-ray light curve is shown in Figure 2, and the unfolded spectra are shown in Figure 3.

2.3. X-Rays: XMM-Newton

Following the prominent rebrightening of ASASSN-15oi at radio frequencies at $\delta t \sim 1400$ days (A. Horesh et al. 2021a), we acquired deep X-ray observations with XMM-Newton (F. Jansen et al. 2001) on 2020 October 8 ($\delta t = 1830$ days; exposure times $\approx$23.6, 23.8, and 12.5 ks for MOS1, MOS2, and pn cameras, respectively; obsID 0872390301; PI Hajela). We acquired additional observations on 2023 April 8 ($\delta t = 2794$ days, exposure times = 21.9, 21.7, and 17.5 ks for MOS1, MOS2, and pn cameras, respectively; obsID 0903330101; PI Hajela). The results from the analysis of the earlier two XMM observations (taken at $\delta t = 76.4$ and $\delta t = 234.5$ days; PI Gezari) were reported in S. Gezari et al. (2017) and T. W. S. Holoien et al. (2018).

All XMM observations were performed with the European Photon Imaging Camera (EPIC) detector in full-frame mode with the thin filter. We processed all of the observations using standard routines in the Scientific Analysis System (SASversion 1.3) software package and the corresponding calibration files. Filtering out time intervals with high background flaring activity results in the net exposure times[32] reported in Table A2.

An X-ray source was clearly detected in three XMM observations at the position of the radio/optical transient. However, there is no evidence of significant emission in the last epoch at $\delta t = 2794$ days. We extracted spectra from a circular region of 15″ (300 pixels) radius centered at the source position, and used a nearby 75″ source-free background region. We performed our spectral analysis using the data from all three EPIC cameras[33] (MOS1, MOS2, and pn).

We fitted the data in the 0.2–12 keV energy range with the same two-component model that we used for Swift-XRT data: `tbabs*ztbabs*(cflux*pow+cflux*bbody)` within XSPEC (v.12.12.1). We did not find evidence for significant intrinsic absorption from a joint fit of the XMM epochs at ~80–1400 days ($N_{\rm H,int} < 1.4 \times 10^{20}\,{\rm cm}^{-2}$), and therefore proceeded with $N_{\rm H,int} = 0$ as before. We used $N_{\rm H,gal} = 5.6 \times 10^{20}\,{\rm cm}^{-2}$ and $N_{\rm H,int} = 0\,{\rm cm}^{-2}$, and report the best-fitting parameters and fluxes in Table A2, plot the light curve in Figure 2, and the unfolded spectra in Figure 3.

Our results are broadly in agreement with those of S. Gezari et al. (2017) with an exception of the power-law X-ray flux that they report as constant with the data available at the time, but we now identify as varying. Additionally, in our new observation at $\delta t = 1833$ days, we find that the blackbody component is not required, and the data are well explained by a nonthermal power-law spectrum only (Figure 3). This result is consistent with our findings from the Swift-XRT spectrum at $\delta t \approx 1400$ days, which was also dominated by the power-law spectral component (Section 2.2). Our latest XMM observation at $\delta t = 2794$ days shows a sharp flux decline as the emission becomes nondetectable.

Taken together, the Swift-XRT and XMM-Newton campaigns lead to the following observational results.[34] (i) While S1 (Section 2.1) falls within the XMM and Swift-XRT point-spread function, we found no evidence for a shift of the centroid of the source of X-ray emission between the second (blackbody dominated) and the third (power-law dominated) XMM epochs. We thus exclude with confidence the possibility that the X-ray power law is associated with S1 and unrelated to the TDE. (ii) Since optical discovery, this transient has radiated $\sim10^{51}$ erg in X-rays. (iii) For $\delta t \lesssim 425$ days, the soft X-ray spectrum consisted of a mixture of a thermal blackbody component with $kT_{\rm BB} \sim 0.05$ keV and a nonthermal power-law component with $\Gamma_{\rm X} \sim 2$, i.e., $F_\nu \propto \nu^{-1}$ (Figure 3). (iv) The brightening of X-ray emission by a factor ≈6 in the time interval $\delta t \approx$ 10–350 days is due to the flux increase of the blackbody component (Figure 2). During this time, the $T_{\rm BB}$ shows no evolution, whereas the effective $R_{\rm BB}$ increases with time from $\sim2.3 \times 10^{11}$ cm to $\sim1.3 \times 10^{12}$ cm. Results (iii)+(iv) confirm the findings of T. W. S. Holoien et al. (2016, 2018) and S. Gezari et al. (2017). (v) Differently from T. W. S. Holoien et al. (2018), we find that the blackbody component rapidly fades between 330 and 425 days and becomes undetectable by the time of the following Swift-XRT observation at $\delta t \approx 1400$ days. (vi) The nonthermal power-law component in the spectra is consistently present, dominates at >1400 days, and shows variability.[35]

2.4. Radio: VLA

A. Horesh et al. (2021a) started monitoring ASASSN-15oi with the VLA at $\delta t = 8$ days. They reported the first radio detection at $\delta t = 182$ days, showing a significant brightening of the source compared to earlier upper limits (Figure 5). The first radio brightening was followed by a second, even more dramatic radio rebrightening at $\delta t > 1400$ days. ASASSN-15oi's second radio flare was discovered in VLASS observations (M. Lacy et al. 2020). It was observed as part of regular survey operations on 2019 July 1 ($\delta t = 1417$ days), revealing a 3 GHz flux density increase of a factor ~3000 since the 2017 observations of A. Horesh et al. (2021a). To further explore the nature of this second radio flare, we obtained multifrequency

---

[32] We note that the slightly different net exposure times in S. Gezari et al. (2017) for the first two observations likely result from different filtering criteria.

[33] S. Gezari et al. (2017) used only observations from EPIC-pn camera. Since the pn detector has the largest number of counts, the results will remain unaffected.

[34] Pre-TDE ROSAT observations of the host galaxy 2MASX J20390918–3045201 provide no useful constraint: T. W. S. Holoien et al. (2018) reported a pre-TDE X-ray flux limit of $F_{\rm X} < 1.9 \times 10^{-12}\,{\rm erg\,cm^{-2}\,s^{-1}}$ (0.1–2.4 keV), which is larger than the measured X-ray fluxes for ASASSN-15oi.

[35] As an example, we compare the XRT count-rate at $\delta t = 1440$ days with the XRT equivalent count-rate of the XMM observation at $\delta t = 1833$ days. Note that both are power-law dominated observations. We find the 0.3–10 keV count-rate to vary significantly at the location of ASASSN-15oi between the observations, while the 0.3-10 keV count-rate of the nearby field source, ≈40″ away, remains consistent.

observations with the VLA under the DDT program 20A-492 (PI: Alexander). The data were taken when the array was in the C configuration at $\delta t = 1741$ days. To monitor the spectral and temporal evolution, we obtained subsequent broadband observations with the VLA under the programs 21A-303 (PI Hajela; $\delta t = 2129$ days) in the B configuration, and 23A-241 (PI Cendes; $\delta t = 2970$ days) in the A configuration. We observed ASASSN-15oi in a standard phase referencing mode for 18–20 minutes at the mean frequencies of 1.5 GHz (*L* band), 3 GHz (*S* band), 6 GHz (*C* band), and 10 GHz (*X* band). We used 8 bit samplers for the *L* and *S* bands and 3 bit samplers for the *C* and *X* bands.

For the observations acquired between $\delta t = 1741$ and 2129 days, we used the VLA calibration pipeline packaged with CASA v.6.2.1.7, with 3C 48 = J0137+3309 as the flux calibrator, and ICRF J210101.6−293327 (J2101−2933) as the complex gain calibrator. For $\delta t = 2970$ days, we used 3C 286 = J1331+3030 as the flux calibrator, the same complex gain calibrator as above, and the new VLA calibration pipeline packaged with CASA v.6.5.4.9. After manually inspecting the data, we further flagged antennas with bad solutions as well as additional weak radio-frequency interference and then reran the pipeline. To densely sample the SED, we divided the data set in every observing band further into sub-bands, and image each sub-band individually using the `CLEAN` algorithm with Briggs weighting and a robust factor of 0.5 in CASA. Where necessary, we also used the automated self-calibration pipeline. We note the presence of a bright source $\sim 0\overset{\circ}{.}3$ away in the 1.5 and 3 GHz bands; however, its residual sidelobes are below the image background rms near ASASSN-15oi. ASASSN-15oi is detected as a bright radio source at all frequencies. We measured the flux density of ASASSN-15oi using the `imtool` package within `pwkit` (P. K. G. Williams et al. 2017) and report the results in Table A3. Since the flux density scale calibration has an accuracy of 3%–5% for our observing bands, we add a conservative 5% systematic uncertainty in quadrature to our uncertainties. We also include this uncertainty in the early-time observations reduced by A. Horesh et al. (2021a).

2.5. Radio: VLBI

We observed ASASSN-15oi with the VLBA of the National Radio Astronomy Observatory (NRAO), using all antennas except Brewster, under the program VLBA/22A-382 (PI: Hajela). The total observing time was 5.5 hr, and the midpoint of the observations was of 2022 February 22.75 (UT; MJD = 59632.75; $\delta t = 2384$ days). We recorded a total bandwidth of 512 MHz, centered on 8.30 GHz, in two circular polarizations, using a total bitrate of 4096 Mbps. The VLBI data were correlated with NRAO's VLBA processor, and the analysis carried out with NRAO's AIPS (Astronomical Image Processing System; E. W. Greisen 2003). The initial flux density calibration was done through measurements of the system temperature at each telescope, and then improved through self-calibration of the phase reference source, which was PMN J2036 − 2830. A correction is made for the dispersive delay due to the ionosphere using the AIPS task `TECOR`, although the effect at our frequency is not large. We phase-referenced the observations of ASASSN-15oi, using a ∼3.7 minute cycle, of which ∼2.5 minutes were on ASASSN-15oi.

We show the VLBI image of ASASSN-15oi, made using the `CLEAN` algorithm, in Figure 4. The total `CLEAN`ed flux density is 1.2 mJy, and the image background rms is 140 μJy beam^{-1}. For an ideal, unresolved source, the peak brightness should also be 1.2 mJy; however, the peak brightness in the image is somewhat larger 1.5 mJy beam^{-1}. So, the relatively low-dynamic-range (11:1) image allows only an approximate determination of the flux density. The angular size of ASASSN-15oi is smaller than our FWHM resolution of 2.47 × 0.78 mas at position angle (p.a.) −5°.

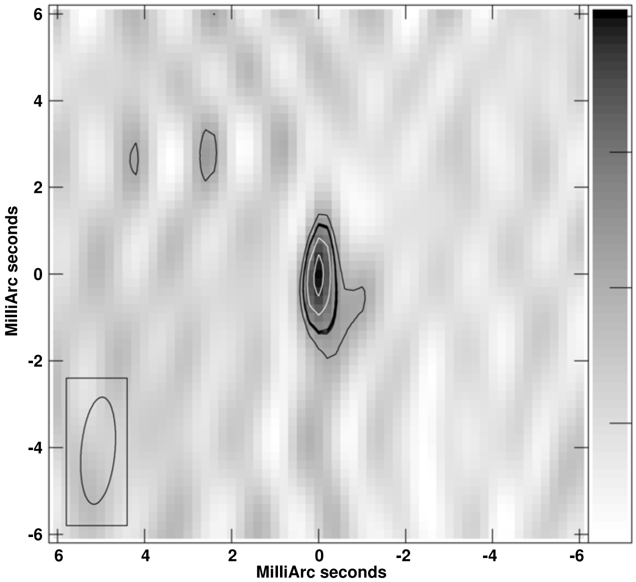

Figure 4. A VLBI image of ASASSN-15oi on 2022 February 22 ($\delta t = 2384$ days), at 8.3 GHz. The peak brightness was 1.5 mJy beam^{-1}, and the image background rms brightness was 140 μJy beam^{-1}. The grayscale is labeled in mJy beam^{-1}. The contours are drawn at −35%, 35%, 50% (emphasized), 70%, and 90% of the peak brightness. The FWHM resolution is shown at the lower left, and was 2.47 × 0.78 mas at p.a. −5°. North is up and east to the left.

For marginally or unresolved sources, such as ASASSN-15oi, the best values or limits for the flux density and source size come from fitting models directly to the visibility data (e.g., M. Bietenholz et al. 2010), rather than from imaging. Fitting a circular Gaussian to the visibilities by least-squares (AIPS task `OMFIT`), we find that the best fit has an FWHM size of 0 ± 1 mas and a flux density of 1.4 ± 0.3 mJy, with the caveat that the fitted size is positively correlated with the fitted flux density. At the distance of ASASSN-15oi, the FWHM translates to a 3σ physical source size of $\sim 9 \times 10^{18}$ cm.

2.6. Radio: ATCA

We acquired observations of ASASSN-15oi (Project code: C3325; PI: Alexander) on 2022 September 30 ($\delta t = 2596$ days) with ATCA. The observations were conducted in the 6D configuration, consisting of all six 22 m diameter antennae (W. E. Wilson et al. 2011). The observing bands were centered at frequencies 2.1, 5.5, and 9 GHz, with a total bandwidth of 2 GHz in each of the bands. For calibration purposes, PKS 1934−638 served as the primary calibrator for all observing bands, whereas PKS 1921−293 (ICRF J202435.5 −325335) was observed in ∼2.5 minute scans enclosing each scan of ASASSN-15oi, and was used as the secondary calibrator to calibrate the time-varying complex gains in the 2.1 GHz (5.5 and 9 GHz) observing band(s).

We carried out the data reduction following the standard calibration procedures in MIRIAD (R. J. Sault et al. 1995), with some additional manual flagging. We split the data into subbands, followed by producing respective dirty images using the task `invert`, and deconvolving the images using the multi-frequency synthesis `CLEAN` algorithm (J. A. Högbom 1974; B. G. Clark 1980; R. J. Sault & M. H. Wieringa 1994). We calculated the flux density by fitting a point-source model to the target in the image plane, and added 10% systematic uncertainty in quadrature to our measurements (S. J. Tingay et al. 2003).

2.7. Radio: MeerKAT

We obtained observations with the MeerKAT radio telescope in the 580–1015 MHz (UHF) and 0.8–2 GHz (*L*) bands on 2022 December 9 (under proposal code SCI-20220822-YC-01, PI: Cendes; δt = 2674 days) and 2023 January 5 (DDD-20220414-YC-01, PI: Cendes; δt = 2701 days). We used ICRF J193925.0−634245 as the flux density calibrator and QSO PKS J2052−3640 as the phase and gain calibrator. We used the calibrated images obtained from the SARAO Science Data Processor pipeline.[36] We measured the flux density of ASASSN-15oi using the `imtool` package within `pwkit` (P. K. G. Williams et al. 2017). Since these observations are close in time to the ATCA observations (Section 2.6) with a mean observation epoch ≈2660 days, we model them together in Section 3.

2.8. Radio: ALMA

Finally, we obtained millimeter-wavelength observations of ASASSN-15oi with ALMA under program 2019.1.01166.T (PI: Alexander). A single epoch of observations at Bands 3 and 6 (mean frequencies 97.5 GHz and 232 GHz, respectively) was obtained on 2022 September 29 (δt = 2128 days). The data were reduced and imaged using the standard NRAO ALMA pipeline in CASA. We add a 3% and 6% systematic uncertainty in quadrature to our Band 3 and Band 6 measurements, respectively.

The radio flux densities are given in Table A3. The radio light curve and SEDs are shown in Figures 5 and 6, respectively. We note that the VLBA measurement of 1.4 ± 0.3 mJy, at 8.30 GHz is lower by 5 ∼ 6σ than the flux densities of 4.7 ± 0.2 and 4.2 ± 0.4 mJy measured with the VLA and ATCA at comparable times and frequencies (Sections 2.4 and 2.6, respectively; see Table A3 and Figure 5). This discrepancy could indicate true radio variability on timescales of ∼300 days at later stages of ASASSN-15oi's evolution; however, a low signal-to-noise ratio (S/N) of the VLBI image (as mentioned in Section 2.5) and a relatively low source decl. (∼−30°) for VLBA[37] may impact this flux density measurement. In addition, since the radio emission measured by other telescopes in the nearby epochs shows a simple trend of t^{-2}, the case of variability is less likely. We therefore, do not include the VLBA measurement in our analysis. To alleviate such issues in the future, we encourage simultaneous observations with the VLBA and other radio telescopes, e.g., VLA, to get full spectral information. We finally also note the discrepancy between the MeerKAT and ATCA data in the 2660 days SED at ∼2 GHz (see Figure 6). However, these are marginally consistent, to within 3σ, and the difference could be due to intercalibration issues between the two telescopes. In the next Section, we model the radio SEDs, and for this particular frequency and epoch, we proceed with assuming 3σ uncertainties on the MeerKAT measurement, instead of the usual 1σ for all others.

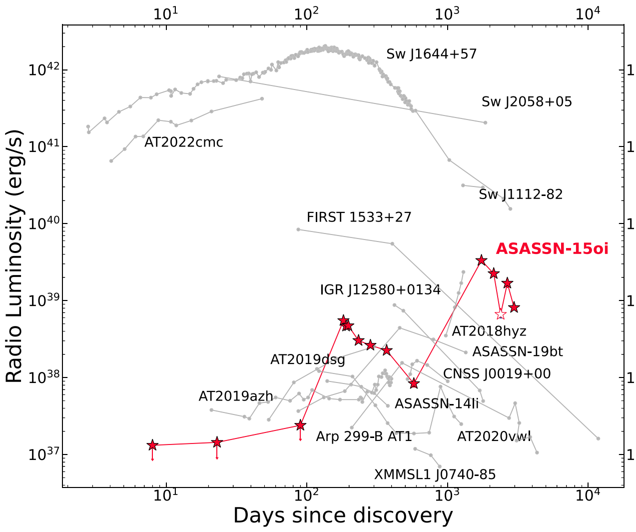

Figure 5. Temporal evolution of the radio luminosity, νL_ν, of ASASSN-15oi (7–8.5 GHz; red stars) compared to selected radio-bright TDEs. The filled red stars show VLA and ATCA measurements, while the VLBA one is shown as an open red star. The other TDEs are: Sw J1644+57 (15.5 GHz compiled from B. A. Zauderer et al. 2011; E. Berger et al. 2012; B. A. Zauderer et al. 2013; T. Eftekhari et al. 2018; Y. Cendes et al. 2021b), AT 2022cmc (11.5 GHz from I. Andreoni et al. 2022) among the jetted TDEs; AT 2018hyz (5–8 GHz from Y. Cendes et al. 2022), AT 2019azh (15.5 GHz from I. Sfaradi et al. 2022), ASASSN-19bt (5.5 GHz from C. T. Christy et al. 2024), and AT 2020vwl (9 GHz from A. J. Goodwin et al. 2023, 2025). The luminosity of the other TDEs has been adopted from K. D. Alexander et al. (2020) in the 3–9 GHz frequency range. At δt ≈ 1800 days, ASASSN-15oi is the most luminous known radio TDE among those not reported to be associated with relativistic jets.

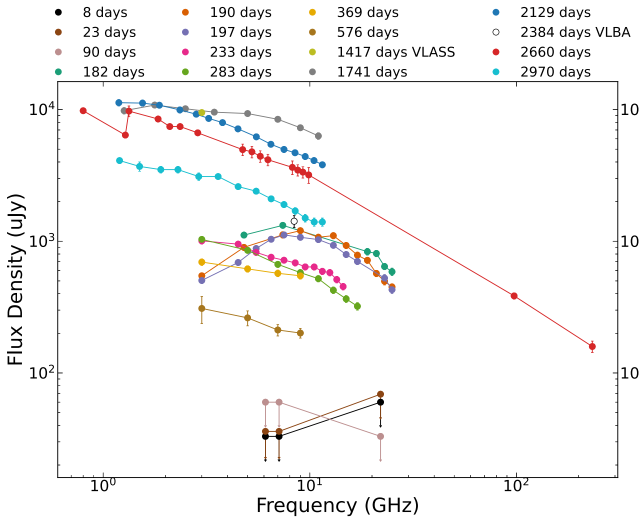

Figure 6. Evolution of the emission from ASASSN-15oi across the radio spectrum from the time of the first radio observation at $\delta t = 8$ days extending to $\delta t = 2970$ days. The data at $\delta t \geqslant 1741$ days are presented here for the first time. All of the flux densities are reported in Table A3. The single-frequency VLASS and VLBA observations are highlighted separately in the plot legend.

---

[36] https://skaafrica.atlassian.net/wiki/spaces/ESDKB/pages/338723406/

[37] https://science.nrao.edu/facilities/vlba/docs/manuals/oss/vlba-decl.-limits

3. Radio Data Modeling

3.1. Fitting of Individual SEDs

We show the radio SEDs of ASASSN-15oi in Figure 6. Spectral evolution is evident, with some SEDs described by a single power law ($F_\nu \propto \nu^\alpha$), and others requiring up to three power-law segments. To fit the SEDs containing *one* break, we use the following parametric model:

$$F_\nu = F_{b_1}\left[\left(\frac{\nu}{\nu_{b_1}}\right)^{\alpha_i/s_1} + \left(\frac{\nu}{\nu_{b_1}}\right)^{\alpha_j/s_1}\right]^{s_1} \tag{1}$$

and to accommodate *two* breaks, we modify the above model as follows:

$$\text{Equation (1)} \times \left[1 + \left(\frac{\nu}{\nu_{b_2}}\right)^{(\alpha_k - \alpha_j)/s_2}\right]^{s_2}, \tag{2}$$

where $\nu_{b_{1,2}}$ are the two break frequencies, $s_{1,2}$ define the sharpness of the two breaks (larger $|s|$ represents a smoother break), and $\alpha_{i,j,k}$ are the power-law indices corresponding to the three spectral segments. Optically thick emission has a spectrum with positive slope ($\alpha > 0$) that we label $\alpha_{\rm thick}$. Optically thin emission has a spectrum with negative slope ($\alpha < 0$) and is labeled with $\alpha_{\rm thin}$. If both of these segments are present, their asymptotic intersection is labeled as $F_{\rm pk}$ and $\nu_{\rm pk}$. If there is an additional break frequency ν_q on the optically thin section of the SED, the power-law index of the steeper segment at higher frequencies is referred to as α_q.

We perform a Markov Chain Monte Carlo (MCMC) fit (using the `emcee` Python package; D. Foreman-Mackey et al. 2013) to the individual radio SEDs. For SEDs featuring both $\alpha_{\rm thin}$ and α_q spectral segments, we introduce an additional constraint to our fitting procedure i.e., $\alpha_q - \alpha_{\rm thin} = -0.5$.[38] We provide the details of the fits and our assumptions in Appendix C in Appendices C.1 and C.2. Due to the complex spectral shapes of the SEDs, we fit them with the above-mentioned models and calculate the Akaike information criterion (AIC) and the Bayesian information criterion (BIC) values for comparison. The details of our model selection are given in Appendix C.3 and Table C1.

We briefly summarize our results for each SED fit here. For the first radio flare SEDs #1, #2, and #3 (see Table 1), we perform a fit with both Equation (1) (as was also done by A. Horesh et al. 2021a) and Equation (2). Based on the AIC and BIC values in Table C1, both fits to these SEDs are statistically equivalent. However, as the fits with Equation (1) have already been presented in A. Horesh et al. (2021a), for exploratory purposes, here we proceed with the best-fitting parameters from Equation (2) (this choice is further supported in Section 3.2.1). We individually fit for $\alpha_{\rm thick,thin}$, $F_{\rm pk}$, $\nu_{\rm pk}$, and ν_q in SEDs #2 and #3, resulting in $\alpha_{\rm thick} \sim +1$. We follow a similar process for SED #1 but fix $\alpha_{\rm thick} = 1$, as there are too few measurements below $\nu_{\rm pk}$ to allow for an independent constraint. The optically thick segments of the SED are similarly not sampled in SEDs #4 and #5. At these epochs, there is a statistically strong preference for Equation (1) fit with the spectral break $\nu_{b_1} = \nu_q$. SEDs #6 and #7 are best fit with a single power law with no breaks.

Table 1
Results of the MCMC Fitting of the Individual Radio SEDs with >2 Data Points

SED #	Epoch (days)	$\alpha_{\rm thick}$	$\alpha_{\rm thin}$	$F_{\rm pk}$ (mJy)	$\nu_{\rm pk}$ (GHz)	ν_q (GHz)
			SEDs associated with the First Radio Flare			
1	182	1	$-0.7^{+0.2}_{-0.2}$	$1.7^{+0.1}_{-0.1}$	$7.1^{+0.9}_{-0.8}$	18^{+8}_{-6}
2	190	$0.8^{+0.1}_{-0.1}$	$-1.0^{+0.1}_{-0.2}$	$1.5^{+0.1}_{-0.1}$	$9.7^{+0.9}_{-0.8}$	17^{+9}_{-3}
3	197	$1.0^{+0.1}_{-0.1}$	$-0.9^{+0.1}_{-0.1}$	$1.4^{+0.1}_{-0.1}$	$8.4^{+0.6}_{-0.5}$	20^{+3}_{-2}
4	233[a,b]	…	$-0.4^{+0.3}_{-0.1}$	>1.0	<3	11^{+2}_{-6}
5	283[a,b]	…	$-0.5^{+0.2}_{-0.1}$	>1.0	<3	9^{+2}_{-4}
6	369[b]	…	$-0.2^{+0.1}_{-0.1}$	>0.7	<3	–[c]
7	576[b]	…	$-0.5^{+0.2}_{-0.2}$	>0.3	<3	–[c]
			SEDs associated with the Second Radio Flare[d]			
8	1741[b]	5/2	$-0.15^{+0.07}_{-0.09}$	<10.8	<1.8	$6.8^{+2.6}_{-1.2}$
9	2129	5/2	$-0.64^{+0.03}_{-0.03}$	19^{+1}_{-1}	$0.9^{+0.1}_{-0.1}$	–[c]
10	2660[b]	5/2	$-0.54^{+0.04}_{-0.04}$	<9.8	< 0.8	16^{+5}_{-4}
11	2970[b]	5/2	$-0.32^{+0.08}_{-0.06}$	<4.1	<1.2	$4.9^{+0.9}_{-1.1}$

Notes. We fit different models to the SEDs and only report the parameters of the preferred model based on the AIC and BIC values reported in Table C1 (see Section 3 for details). For all SEDs except that at $\delta t = 2129$, we assume $s = -0.3$, and $s_2 = -0.003$; at $\delta t = 2129$ days, we use $s = -1$ to accommodate the broader peak of the SED. Where ν_q is identified, we use $\alpha_q = \alpha_{\rm thin} - 0.5$. The central values reported here are the medians of the posterior distributions, and the uncertainties are at the 68% confidence level.

[a] These SEDs show no low-frequency turnover, but show a steepening at high frequencies. We therefore fit them with Equation (1), where the two spectral indices are given by $\alpha_{\rm thin}$ and $\alpha_{\rm q} = \alpha_{\rm thin} - 0.5$.

[b] In these SEDs, we use the maximum observed F_ν, and the corresponding frequency as the limits on $F_{\rm pk}$ and $\nu_{\rm pk}$.

[c] ν_q is not observed in these SEDs.

[d] For these SEDs, the optically thick part of the spectrum cannot be constrained. We fix $\alpha_{\rm thick} = 5/2$.

For the second radio flare (Appendix C.2) SEDs, there is no evidence for optically thick emission at the observed frequencies, and therefore, we fix $\alpha_{\rm thick} = 5/2$, as is typically done for TDEs. Equation (2) is the statistically preferred model for SEDs #8, #10, and #11, while Equation (1) is preferred for SED #9.

A peak can only be constrained for SEDs #1, #2, #3, and #9. For every other SED (#4, #5, #6, #7, #8, #10, and #11) where a peak cannot be constrained, we assume a lower limit on $F_{\rm pk}$ and an upper limit on $\nu_{\rm pk}$ as the maximum observed flux density and its corresponding frequency, respectively. We report the best-fitting parameters for all SEDs in Table 1, present the fits in Figure 7, and show the evolution of the SED peaks and ν_q in Figure 8.

3.2. Equipartition Physical Parameters from a Quasi-spherical Outflow Model

Using the inferred $F_{\rm pk}$, $\nu_{\rm pk}$, and $\alpha_{\rm thin}$, we can now estimate the physical parameters of the outflow responsible for the radio emission. To that end, we adopt a synchrotron self-absorption (SSA) model given by R. A. Chevalier (1998), as commonly used in the TDE literature (e.g., K. D. Alexander et al. 2020 and references therein). This model assumes that the synchrotron radiation is powered by relativistic electrons accelerated by a shock interacting with the ambient medium, resulting in a

---

[38] This assumption is valid for the physical models used in Sections 3.2 and 3.3.

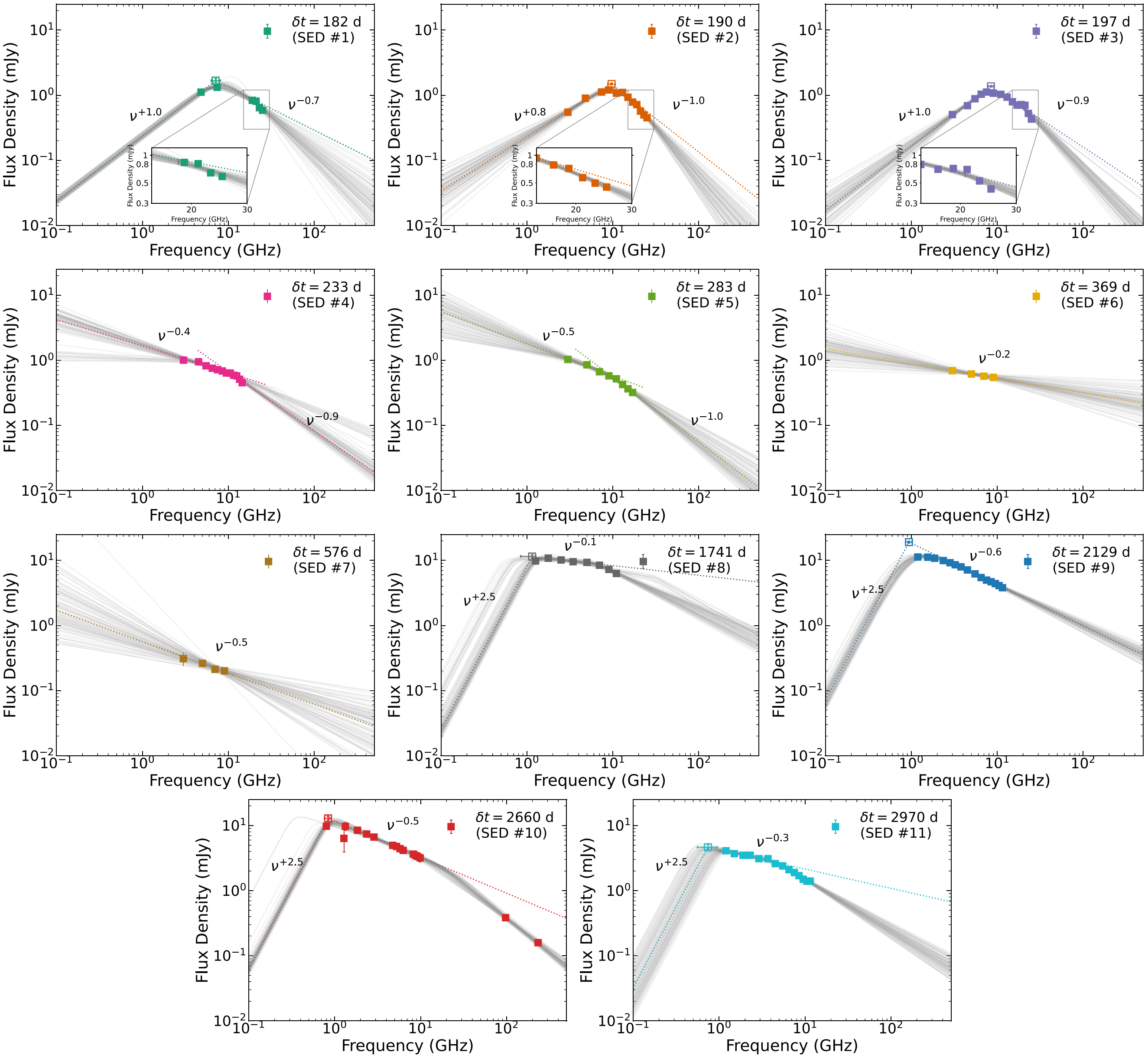

Figure 7. Radio SEDs of ASASSN-15oi and the best-fitting models: SEDs #1, #2, #3, #8, #10, and #11 are fitted with Equation (2), and SEDs #4, #5, and #9 are fitted with Equation (1), while SEDs #6 and #7 are fitted with a single power law. The solid gray curves are a selection of 50 models randomly sampled from the posterior distribution. Where applicable, dotted lines show the asymptotic power laws with the best-fitting spectral indices (the medians of the posterior distributions), and the empty squares are the intersection of the $\alpha_{\rm thick}$ and $\alpha_{\rm thin}$ segments in the respective SEDs. For clarity, we have also zoomed-in on the frequencies around ν_q in some SEDs.

broadband SED. At $\nu < \nu_{\rm pk}$, the synchrotron radiation is self-absorbed resulting in $F_\nu \propto \nu^{5/2}$. At $\nu > \nu_{\rm pk}$, the spectrum becomes optically thin and follows $F_\nu \propto \nu^{-(p-1)/2}$, where p is the power-law index of the population of accelerated electrons. In the context of our model parameters in Section 3.1, the spectral indices become $\alpha_{\rm thick} = 5/2$ and $\alpha_{\rm thin} = -(p-1)/2$. The indices p derived from the best-fitting $\alpha_{\rm thin}$ for each SED are reported in Table 2. Noticeably, the value of p *changes* abruptly between epochs, which is unphysical for a single population of radiating electrons, suggesting the presence of multiple synchrotron sources instead. This interpretation will be corroborated further as we proceed with our analysis.

For SEDs #1, #2, and #3, we have $\alpha_{\rm thick} \sim 1 \neq 5/2$. A shallow optically thick slope can possibly be explained by a clumpy medium (e.g., K. W. Weiler et al. 2002; C. I. Björnsson & S. T. Keshavarzi 2017), a possibility also explored by A. Horesh et al. (2021a). The inhomogeneity of a clumpy medium results in superposition of several SSA spectra with different peaks. In this case, the physical parameters derived from the R. A. Chevalier (1998) analysis are representative of the population of electrons that dominate the peak of the SED.

We adopt a volume filling factor of $f = 0.5$ in the equations presented in L. DeMarchi et al. (2022) to constrain the post-shock magnetic field B, the radius of the emitting region R, the internal energy U, the electron number density of the ambient medium n_e, and the average velocity of the shock as $v = R/\delta t$. The equations in L. DeMarchi et al. (2022) generalize those originally presented in R. A. Chevalier (1998) for an arbitrary value of p (see also R. A. Chevalier & C. Fransson 2017). The expressions for B, R, U, and n_e are presented in Appendix E.

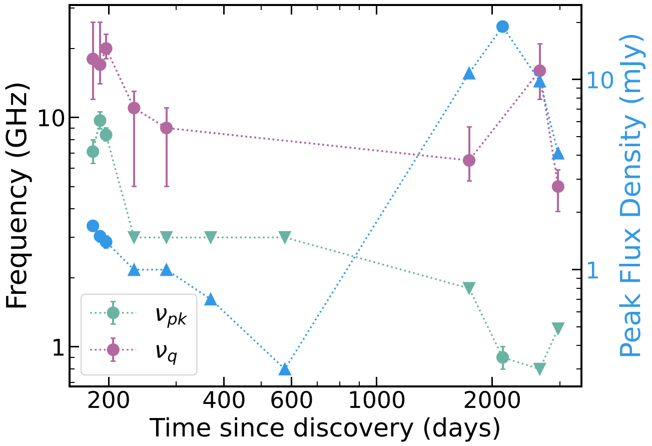

Figure 8. The evolution of the $F_{\rm pk}$, $\nu_{\rm pk}$, and ν_q with time.

Equations (E1)–(E4) are derived assuming $\gamma_{\rm max} \to \infty$, where $\gamma_{\rm max}$ is the maximum Lorentz factor attained by the electrons accelerated by the shock. In this case, for the energy density in the electrons to be finite, $p > 2$ is required. Conversely, a $p < 2$ requires finite $\gamma_{\rm max}$. We derive equations for the $p < 2$ regime in Appendix F. The multidimensional particle-in-cell simulations suggest $\gamma_{\rm max} \lesssim 10^8$ (L. Sironi et al. 2013). Here, we assume $\gamma_{\rm max} = 10^3$ (with these electrons emitting synchrotron radiation at ∼3 THz for a nonrelativistic shock). We note that B, R, and U are proportional to $\gamma_{\rm max}$, and the estimates of the physical parameters can vary significantly with changing $\gamma_{\rm max}$, when $1 \lesssim p \ll 2$.

As this model has many free parameters, a unique solution is generally only possible if multiple spectral breaks of the synchrotron spectra can be measured directly from the data. In the absence of other constraints, the system is assumed to be in equipartition; i.e., the fraction of internal energy in the relativistic electrons ($\epsilon_{\rm e}$) is equal to the fraction of internal energy of the post-shock magnetic field ($\epsilon_{\rm B}$), where $\epsilon_{\rm e} = \epsilon_{\rm B} = 0.1$. We note that there is no observational support for such a choice, but this is a standard assumption in the field. This enables us to estimate the physical parameters of the synchrotron-emitting region even if only $F_{\rm pk}$, $\nu_{\rm pk}$, and p can be measured directly. Where the peak was not constrained, the limits on $F_{\rm pk}$ and $\nu_{\rm pk}$ translate into limits on the inferred physical quantities. We denote parameters (X) that are calculated assuming equipartition conditions as $X_{\rm eq}$.

The resulting values are reported in Table 2, and the evolution of these parameters is shown in Figure 9. We note the dramatic increase in the inferred energy between the two flares from $U_{\rm eq} \sim 10^{49}$ erg at $\delta t = 182$ days to $U_{\rm eq} \sim 10^{51}$ erg at $\delta t = 2129$ days. This implies that a different, more powerful energy source is needed to explain the second radio flare. We explore a scenario of a relativistic jet as a source of emission for the second radio flare in Section 3.3. In the next Section, we briefly discuss the inferences that can be drawn if we assume that ν_q is the synchrotron cooling break.

3.2.1. Synchrotron Cooling Break

We can relax the assumption of equipartition, i.e., partially break the degeneracy between ϵ_e and ϵ_B, if we can measure another characteristic of the synchrotron spectrum, such as the synchrotron cooling break $\nu_{\rm cool}$. This would enable a more accurate estimate of the outflow parameters. For ASASSN-15oi, the break ν_q constrained in Section 3.1 for some SEDs may be interpreted as $\nu_{\rm cool}$.

For a nonrelativistic shock, $\nu_{\rm cool}$ is calculated as:

$$\nu_{\rm cool} = \frac{18\pi m_{\rm e} c q_{\rm e}}{\sigma_T^2 {B_c}^3 (t_{\rm dyn})^2} \tag{3}$$

where $m_{\rm e}$ and $q_{\rm e}$ are the mass and the charge of the electron, c is the speed of light, σ_T is the Thomson cross section, B_c is the magnetic field, and $t_{\rm dyn}$ is the dynamical time. Note that we represent the physical parameters here as X_c, to differentiate these estimates from the equipartition ones above.

We selected the models with two break frequencies for SEDs #1, #2, and #3 in Section 3.1. The second break constrained in these SEDs could correspond to the synchrotron cooling frequency. To verify this, we assume $t_{\rm dyn} = \delta t$ and $B_c = B_{\rm eq}$ in Equation (3), and find that $\nu_{\rm cool} \approx \nu_q$ within 1σ for SEDs #2 and #3 and within 3σ for SED #1. While this result supports the hypothesis that there may be two break frequencies in these SEDs and aligns with the initial equipartition assumption, we note that the uncertainties on the best-fitting ν_q are large, preventing us from conclusively claiming them as synchrotron cooling breaks.

We fitted for ν_q in SEDs #4, #5, #8, #10, and #11 in Section 3.1. For each of these SEDs, if we assume, $t_{\rm dyn} = \delta t$ and $\nu_{\rm cool} = \nu_q$, the measured B_c from Equation (3) (in Table 3) is different from $B_{\rm eq}$ in Table 2, in contrast to SEDs #1, #2, and #3. Using B_c, we can solve for $\epsilon_{{\rm B},c}/\epsilon_{{\rm e},c}$ using Equation (E1) or (F3), depending on p. With our initial assumption of $\epsilon_{{\rm e},c} = 0.1$, we obtain $\epsilon_{{\rm B},c} > 1$. This is clearly unphysical. Smaller values of $\epsilon_{{\rm e},c}$ (specifically $10^{-4} \leqslant \epsilon_{{\rm e},c} < 0.1$) would yield acceptable $\epsilon_{{\rm B},c}$ values. Here, we adopt $\epsilon_{{\rm e},c} \geqslant 10^{-4}$, where this lower bound is set by the simulations in, e.g., J. Park et al. (2015) for nonrelativistic collisionless shocks. The upper bound on $\epsilon_{{\rm e},c}$ is set by the condition $\epsilon_{{\rm B},c} < 1$. Both B_c and the allowed range of $\epsilon_{{\rm B},c}$ are reported in Table 3. As can be seen from Table 3, our choices yield extreme ratios of the microphysical shock parameters $\epsilon_{{\rm B},c}/\epsilon_{{\rm e},c} \lesssim 500$.

Our analysis of the radio emission, based on the R. A. Chevalier (1998) model, suggests that $\nu_{\rm q}$ constrained here are unlikely to be synchrotron cooling breaks. Furthermore, the changes in p and shallow $\alpha_{\rm thin}$ found in most of these SEDs hint at a contribution from multiple synchrotron spectra. Several SSA spectra with different p values can superimpose to produce a shallow ($p < 2$) optically thin segment, e.g., as seen in some AGNs (K. I. Kellermann & I. I. K. Pauliny-Toth 1969). This may indeed be true, as α_q in SEDs #4, #5, #8, #10, and #11 resembles $\alpha_{\rm thin}$ expected from a standard SSA spectrum, i.e., instead of $\nu_{\rm q}$ representing a synchrotron cooling break, it may simply represent a transition to frequencies where a single synchrotron spectrum begins to dominate. In other words, while multiple synchrotron sources may dominate the spectra at $\nu < \nu_{\rm q}$, a single synchrotron component emerges at $\nu > \nu_{\rm q}$. Finally, the steep jumps, particularly in the inferred density $n_{\rm e,eq}$ between $\delta t \approx 197$ days and 233 days also suggest an inhomogeneous medium. Therefore, a likely unified scenario that can explain both the peculiar SED properties and the abrupt jumps in the physical parameters is that of multiple outflows launched in an inhomogeneous medium. We discuss this scenario further in Section 4.2.

Table 2

Physical Parameters Inferred from the Equipartition Modeling of the Radio Data, Detailed in Section 3, Assuming $\epsilon_e = \epsilon_B = 0.1$

SED #	δt (days)	p	$B_{\rm eq}$ (G)	$U_{\rm eq}$ ($\times 10^{49}$ erg)	R_{eq} ($\times 10^{16}$ cm)	$n_{\rm e,eq}$ ($\times 10^3$ cm^{-3})	$v_{\rm eq}$[a] ($\times$Speed of Light)
Modeling of SEDs associated with the First Radio Flare							
1	182	$2.3^{+0.3}_{-0.3}$	$0.41^{+0.08}_{-0.06}$	$0.9^{+0.5}_{-0.2}$	$4.0^{+0.3}_{-0.3}$	9^{+4}_{-2}	$0.084^{+0.007}_{-0.006}$
2	190	$3.0^{+0.5}_{-0.3}$	$0.74^{+0.34}_{-0.18}$	$1.9^{+3.5}_{-0.9}$	$3.5^{+0.4}_{-0.3}$	38^{+30}_{-16}	$0.070^{+0.006}_{-0.007}$
3	197	$2.7^{+0.2}_{-0.2}$	$0.55^{+0.09}_{-0.08}$	$1.0^{+0.5}_{-0.3}$	$3.4^{+0.2}_{-0.2}$	24^{+9}_{-6}	$0.066^{+0.003}_{-0.003}$
4	233	$\sim$1.8	<0.16	>0.45	>6.0	<0.9	>0.1
5	283	$\sim$1.9	<0.16	>0.54	>6.3	<1.2	>0.1
6	369	$\sim$1.4	<0.18	>0.25	>4.4	<5.4	>0.04
7	576	$\sim$1.9	<0.18	>0.13	>3.6	<20	>0.02
Modeling of SEDs associated with the Second Radio Flare							
8	1741	$1.3^{+0.2}_{-0.1}$	<0.08	>9	>26	<0.72	>0.06
9	2129	$2.2^{+0.1}_{-0.1}$	$0.04^{+0.01}_{-0.01}$	93^{+9}_{-6}	90^{+8}_{-5}	$0.02^{+0.01}_{-0.01}$	$0.16^{+0.01}_{-0.01}$
10	2660	$2.1^{+0.1}_{-0.1}$	<0.04	>52	>75	<0.04	>0.10
11	2970	$1.6^{+0.1}_{-0.2}$	<0.06	>6	>27	<0.89	>0.03

Notes. Here, p is derived from $\alpha_{\rm thin}$ resulting from the MCMC fitting of the observed SEDs. $\alpha_{\rm thin}$, $F_{\rm pk}$, and $\nu_{\rm pk}$ values reported in Table 1 are used to derive the physical parameters according to the model described by R. A. Chevalier (1998). The derivations of the physical parameters in Equations (E1)–(E4) are dependent on $p > 2$. For SEDs with $p < 2$, we use Equations (F3)–(F5). The values in the table are sensitive to $F_{\rm pk}$, and $\nu_{\rm pk}$, which depend on $\alpha_{\rm thin,thick}$, and therefore to how smoothly the power laws are joined in the broken power-law model (i.e., to the value of $|s|$).

[a] The velocity is measured with respect to days since the optical discovery. We note that velocities of the outflow at one epoch relative to the other epoch can be calculated as $\Delta R/\Delta t$.

3.3. Physical Parameters from an Off-axis Relativistic Jet

Here, we examine if an off-axis relativistic jet could power the second radio flare at $\delta t \gtrsim 1400$ days. This scenario is commonly invoked for explaining the delayed radio emission in TDEs (see, e.g., Y. Cendes et al. 2022; E. S. Perlman et al. 2022; T. Matsumoto & T. Piran 2023; C. T. Christy et al. 2024; I. Sfaradi et al. 2024). T. Matsumoto & T. Piran (2023) provided a generalized treatment of jets viewed at arbitrary angles in the context of TDEs. Compared to the R. A. Chevalier (1998) model, in a jetted relativistic regime, three additional variables come into play: the jet Lorentz factor, Γ, the jet opening angle $\theta_{\rm jet}$, and the viewing angle, $\theta_{\rm obs}$, i.e., the angle between the jet axis and the observer's line of sight. The jet energy per solid angle is assumed to be constant for $\theta < \theta_{\rm jet}$ and 0 at larger angles (a so-called "top-hat" jet). The equations derived in T. Matsumoto & T. Piran (2023) are applicable for a system in equipartition, and we follow C. T. Christy et al. (2024) to incorporate the corrections outlined in R. Barniol Duran et al. (2013) for a more general system. Proceeding as in Section 3.2.1 and assuming our measured high-frequency break (ν_q) as the relativistic synchrotron cooling break ($\nu_{\rm cool,jet}$), allows us to relax the assumption of equipartition. This results in $\epsilon_{\rm B,jet} < 1$ for $\epsilon_{\rm e,jet} = 0.1$, reported in Table 4, in contrast to the nonrelativistic uncollimated blastwave scenario.

Here, we consider a dynamically spreading jet whose opening angle $\theta_{\rm jet} = 1/\Gamma$ grows as the jet decelerates. This is equivalent to considering only the energy within an angle of $1/\Gamma$ from our line of sight. As material at larger angles has a negligible contribution to the observed emission due to relativistic beaming, this provides the minimum energy necessary to explain our observations at each epoch. In contrast, a narrow jet with constant opening angle $\theta_{\rm jet} \sim 10°$ (typical of AGN jets), which is more physically likely, would require higher Lorentz factors and correspondingly larger emission radii to produce the same observed emission.

As T. Matsumoto & T. Piran (2023) analysis only applies for $p > 2$, we perform this analysis only on the $\delta t = 2129$ and 2660 day SEDs. For the $\theta_{\rm jet} \geqslant 1/\Gamma$ case, we calculate the radius that minimizes the total energy under a $p = 2.1$ power-law distribution of electrons (resulting from the best-fitting $\alpha_{\rm thin}$ in Section 3.1). We assume equipartition, with $\epsilon_{\rm e,jet} = \epsilon_{\rm B,jet} = 0.1$ for the 2129 day SED and break the degeneracy in the 2660 day SED using the constrained $\nu_{\rm cool,jet}$. We carry out the MCMC analysis as before, and all of the best-fitting values are reported in Table 4 for two illustrative scenarios: a promptly launched jet with $t_{\rm dyn} = \delta t$ (top rows) and a delayed jet launched with $t_{\rm dyn} = \delta t - 1471$ days (bottom rows). Here, the delayed jet's launch date is chosen to be the time of the first detection of the second flare; the true launch date is presumably between these two extremes. Times measured since these jet launch dates are represented as $\delta t_{\rm jet}$. For each launch date, we also consider two possible observer viewing angles: $\theta_{\rm obs} = 30°$ and $\theta_{\rm obs} = 90°$.

Now we discuss the fitting results and the associated caveats. For the most off-axis case ($\theta_{\rm obs} \approx 90\circ$) at the latest possible jet launch time, the jet models require $\Gamma \gtrsim 3$. This is an unusually large Lorentz factor for an outflow ~4 yr after its launch, given the high-density nuclear environments in which TDEs occur. The required jet energy is also high in most cases ($U_{\rm jet} \gtrsim 10^{52}$ erg, Table 4), but is similar to the energies previously inferred for radio-luminous TDEs with powerful on-axis relativistic jets (e.g., E. Berger et al. 2012; S. B. Cenko et al. 2012; B. A. Zauderer et al. 2013; G. C. Brown et al. 2015). Note that the lowest energy is inferred for the $\delta t_{\rm jet} = 658$ days SED with $\theta_{\rm obs} = 90°$, but this is the equipartition energy; if the system is not in equipartition, the true energy will be even higher. With the equipartition $R_{\rm jet}$ and Γ for this epoch, the emitting region has a transverse size of $R_{\rm jet}/\Gamma \sim 6 \times 10^{17}$ cm. Our VLBA observation at =2384 days in Section 2.5 gives a 3σ upper limit to the physical source size of 9×10^{18} cm, which is not constraining. The less off-axis cases all require even higher jet Lorentz factors, which we

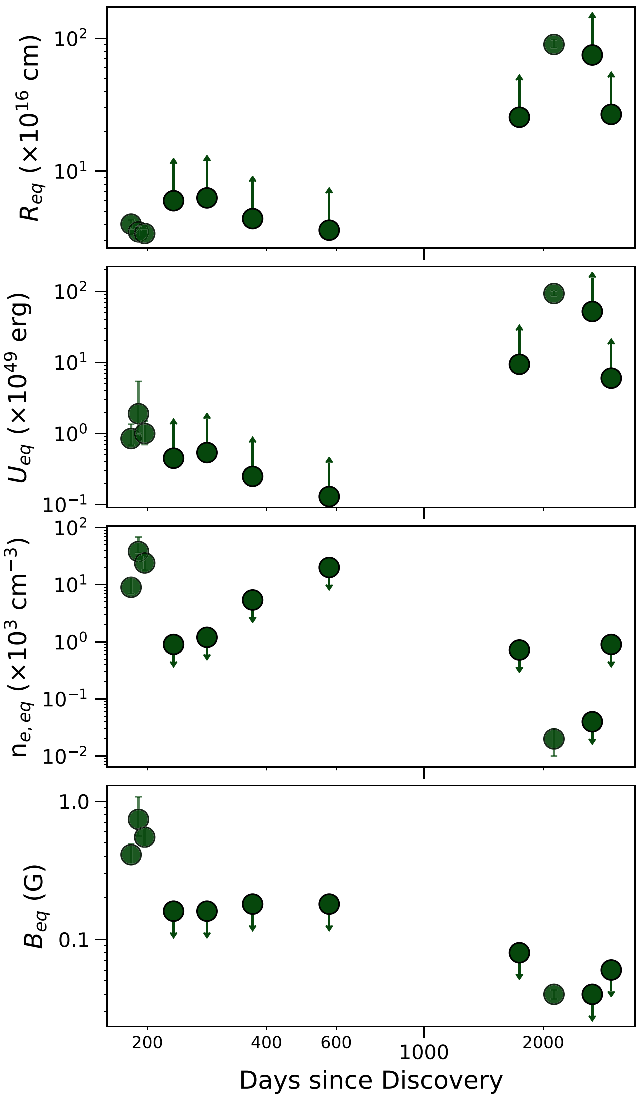

Figure 9. Physical parameters from the modeling of the radio data assuming equipartition. The dramatic jumps in the magnetic field and density estimate from the SEDs within the first radio flare suggest an inhomogeneous medium, or multiple synchrotron sources. A significant jump between the energy inferred for the first and second radio flare hints at two distinct sources of emission for the two flares.

Table 3
We Determine B_c from Equation (3), Then Solve for $\epsilon_{B,c}$ from Equation (E1) or (F3), Assuming $\epsilon_{e,c} \geqslant 10^{-4}$ as Long as the Resulting $\epsilon_{B,c} < 1$

SED #	δt (days)	B_c (G)	$\epsilon_{B,c}$
1	182	0.72	$\approx \epsilon_{e,c}$
2	190	0.73	$\approx \epsilon_{e,c}$
3	197	0.66	$\approx \epsilon_{e,c}$
4	233	0.72	$\geqslant$0.052
5	283	0.68	$\geqslant$0.045
8	1741	0.23	$\geqslant$0.005
10	2660	0.12	$\geqslant$0.018
11	2970	0.17	$\geqslant$0.009

consider to be physically unlikely. Furthermore, if the emission was powered by an off-axis jet, $\Gamma_{\rm jet}$ is expected to decrease with time. However, in Table 4, we do not see such a trend. A single-component top-hat jet is thus unlikely to explain the second radio flare of ASASSN-15oi.

4. Discussion

Figure 10 shows the contemporaneous evolution of emission from ASASSN-15oi across all of our observed wavelengths. Here is a brief overview of how the luminosity changes over time at each wavelength:

1. The UV/optical (UVO) bolometric luminosity ($L_{\rm UVO,bol}$) remains stable for the first ∼50 d (with the luminosity consistent within 1σ) and subsequently shows a steep decline. It plateaus starting at $\delta t \approx 200$ days for ∼100 days before the optical luminosity fades to the host galaxy level. In contrast, the UV luminosity continues to plateau out to ∼3000 days at values in excess of the host galaxy emission.
2. The X-ray luminosity has two components characterized by a blackbody and a power-law spectrum, respectively. The X-ray blackbody flux shows little to no variation for the first ∼80 days. Over the following ∼150 days, it brightens significantly by a factor of ∼6, accompanied by an increase in $R_{\rm BB}$ but not $T_{\rm BB}$. Similar to the UVO emission, the X-ray blackbody flux shows little variation from $\delta t \sim 200$ to 300 days. The blackbody X-rays then fade to nondetectable levels at $\delta t > 1400$ days.
3. The top panel of Figure 10 shows the total observed thermal bolometric luminosity, $L_{\rm bol} = L_{\rm UVO,bol} + L_{\rm X,BB,bol}$, where $L_{\rm UVO,bol}$ is adopted from J. T. Hinkle et al. (2021) and $L_{\rm X,BB,bol}$ is calculated using the best-fitting $R_{\rm BB}$ and $T_{\rm BB}$ in Table A2. As can be seen, the thermal bolometric luminosity remains constant during the period $\delta t \sim$ 80–230 days before abruptly declining. The UVO and blackbody X-ray luminosities show opposite trends between ∼80 and 230 days, and add up to a constant $L_{\rm bol}$, suggesting that the UVO and blackbody X-ray emission are related.
4. The power-law X-ray emission is variable. The power-law component shows a factor of ∼4 increase in the 0.3–10 keV flux between 234 days and 425 days. At $\delta t > 1440$ days, X-rays fluctuate more dramatically, varying by a factor of ∼9. In our last observation, the luminosity declines by a factor of ∼7 fading below detectable levels after $\delta t \approx 2580$ days.
5. In radio, ASASSN-15oi exhibits *two* distinct flares, with the first radio detection at $\delta t = 182$ days. It rises from the earlier nondetections as $F_\nu \propto t^{4.5}$ and subsequently declines as $\sim t^{-1}$.
6. The second radio flare was first detected at $\delta t = 1471$ days (with a rise of $\sim t^4$ from the last observation of the first flare) and subsequently fades $\propto t^{-1.5}$ from $\delta t \gtrsim 1741$ to 2660 days. Between the 2660 day and 2970 day observations, the light curve declines steeply as t^{-7}.

Observations at UVO wavelengths and the blackbody component of the X-ray radiation can be best described as thermal emission with maximum temperatures of $\approx 5 \times 10^4$ K, and $\approx 6 \times 10^5$ K, respectively. The associated radius of the thermal X-ray emission is $\sim$(2–13) $\times$ 10^{11} cm, which is comparable to the inner regions ($\lesssim 4 r_g$) of an accretion disk around an $M_{\rm BH} = 2.5 \times 10^6 M_\odot$ nonrotating SMBH. This $M_{\rm BH}$ was reported by S. Gezari et al. (2017), and we adopt this value

Table 4
Physical Parameters Derived from the Off-axis Jet Model of Section 3.3

SED #	$\delta t_{\rm jet}$ (days)	$\theta_{\rm obs}$ (°)	$\epsilon_{\rm B,jet}$	$B_{\rm jet}$ (G)	$U_{\rm jet}$ ($\times 10^{52}$ erg)	$R_{\rm jet}$ ($\times 10^{18}$ cm)	$n_{\rm e,jet}$ (cm^{-3})	$\Gamma_{\rm jet}$	$R_{\rm jet}/\Gamma$ ($\times 10^{17}$ cm)[a]
Times measured as days since discovery									
9	2129[b]	30	0.1	$0.22^{+0.02}_{-0.02}$	$33.7^{+3.7}_{-3.4}$	$49.5^{+0.1}_{-0.1}$	$0.15^{+0.06}_{-0.04}$	59^{+4}_{-5}	∼8.4
10	2660[c]	30	0.003	<0.04	>51	>37.1	>0.3	>41	∼9.0
9	2129[b]	90	0.1	$0.25^{+0.03}_{-0.03}$	$6.0^{+0.5}_{-0.6}$	$6.58^{+0.02}_{-0.02}$	$0.9^{+0.2}_{-0.2}$	8^{+1}_{-1}	∼8.6
10	2660[c]	90	0.015	<0.07	>5.2	>6.24	>0.8	>6	∼1.0
Times measured as days elapsed since $T_0 = 1471$ days									
9	658[b]	30	0.1	$0.14^{+0.01}_{-0.01}$	$2.0^{+0.2}_{-0.2}$	$15.23^{+0.03}_{-0.03}$	$0.13^{+0.04}_{-0.03}$	25^{+2}_{-2}	∼6.0
10	1189[c]	30	0.051	<0.07	>4.7	>24.9	>0.1	>26	∼9.6
9	658[b]	90	0.1	$0.15^{+0.02}_{-0.02}$	$0.32^{+0.03}_{-0.04}$	$1.94^{+0.02}_{-0.02}$	$0.7^{+0.2}_{-0.2}$	$3.2^{+0.2}_{-0.3}$	∼6.1
10	1189[c]	90	0.293	<0.14	>1	>4.1	>0.1	> 4	∼1.0

Notes.

[a] This column gives the transverse size of the emitting region. As can be seen, the VLBA 3σ upper limit on the source size of 9×10^{18} cm is nonconstraining in all of the cases.

[b] As no ν_q is observed for this SED, we assume equipartition, and note that any deviation from equipartition will result in an increase in the energy and density estimate.

[c] Here, we break the degeneracy between the microphysical parameters using $\nu_q = \nu_{\rm cool,jet}$ and $\epsilon_{\rm e,jet} = 0.1$ to solve for $\epsilon_{\rm B,jet}$t.

for our subsequent analysis.[39] The UVO emission originates from a region extending out to $\sim 10^{15}$ cm $> > r_g$. Conversely, both the emission detected at radio wavelengths, and the contribution of the power-law component to the observed X-rays, can be characterized as nonthermal. Below we discuss the possible physical origin of each emission component.

4.1. Thermal Emission from ASASSN-15oi as Explained by the "Cooling Envelope" Model

In a previous investigation of ASASSN-15oi (S. Gezari et al. 2017) that extended to $\delta t \sim 600$ days, it was suggested that the prompt UVO emission originated in shocks resulting from stream–stream collisions during the process of circularization, but owing to inefficiencies in this process, the formation of the accretion disk was postponed, causing a delayed rise in thermal X-rays (at $\delta t \sim 100$ days). Motivated by point Nos. 1, 2, and 3 in the above list, we explore an alternate scenario of a cooling envelope model proposed by B. D. Metzger (2022), where the UVO and thermal X-rays can be explained in a unified scenario. It is similar to the assumptions made by S. Gezari et al. (2017) in that the accretion is delayed. However, the difference is that in the cooling envelope model, the debris circularizes promptly and efficiently (e.g., as seen in recent simulations; E. Steinberg & N. C. Stone 2024), and forms a quasi-spherical pressure-supported envelope. The envelope undergoes Kelvin–Helmholtz contraction and cools radiatively, resulting in a fading UV and optical luminosity, as observed. As the envelope is contracting, material is gradually accreted onto the SMBH causing the delayed rise in the X-rays. This scenario is appealing for explaining the decline in the UV/optical bolometric luminosity together with the rise in thermal X-ray emission and the subsequent UV/optical/X-ray luminosity plateaus.

Specifically, in the cooling envelope model, the debris stream promptly circularizes on the fallback timescale of the most tightly bound debris according to

$$t_{\rm fb} \simeq 41\ {\rm days} \left(\frac{k}{0.8}\right)^{-3/2} M_{\rm BH,6}^{1/2}\, m_*^{1/5} \tag{4}$$

where k is the constant related to stellar structure and rotation prior to disruption, and is taken as $k = 0.8$ for a $\gamma = 5/3$ polytropic star (as assumed in B. D. Metzger 2022); $M_{\rm BH,6}$ is the mass of the SMBH in units of $10^6 M_\odot$, and $M_* = m_* M_\odot$ is the mass of the disrupted star. Assuming that the disruption occurs at the time of the optical discovery, when a star with mass $m_* = 1\, M_\odot$ is disrupted on a path with a penetration factor $\beta = 1$ (with $k \simeq 0.8$), a pressure-supported quasi-spherical envelope is formed at $t_{\rm fb} \approx 60$ days [40] (plotted with the gray dotted line in Figure 10).

The cooling envelope model predicts an initial photospheric radius of $R_{\rm ph} \approx 6 \times 10^{14}$ cm (Equation (17) in B. D. Metzger 2022), similar to the observed $R_{\rm ph} \sim 2 \times 10^{14}$ cm of the optical emission from J. T. Hinkle et al. (2021) at $t = t_{\rm fb}$. The initial optical luminosity of 2.5×10^{43} erg s^{-1} at $\nu = 6.8 \times 10^{14}$ Hz predicted by this model (given by their Equation (32) for mass estimates used here) is in good agreement with the observed optical luminosity of $\sim 1.5 \times 10^{43}$ erg s^{-1} at $t = t_{\rm fb}$. As the envelope contracts, the optical luminosity decreases while the accretion rate increases, leading to a delayed rise in the X-rays. We see both the decrease in optical luminosity and rise in X-ray luminosity over a period of $\sim$150 days.[41]

If there is sufficient energy feedback from accretion, the envelope remains "puffed up," i.e., depending on how

---

[39] We provide other host SMBH mass estimates of ASASSN-15oi that have been reported in the literature in Appendix G, and note that using these other estimates has no major impact on our conclusions.

[40] If the timescale of envelope formation, and hence $t_{\rm fb}$, is the same as the time at which the UVO luminosity starts decaying at $t = 45$ days, the disrupted star will have $m_* \approx 0.2\, M_\odot$. On the other hand, if we assume $m_* = 1\, M_\odot$, we get $M_{\rm BH} \approx 1.2 \times 10^6\, M_\odot$, lower than most of the mass estimates in the literature, but consistent with the studies by T. Wevers et al. (2019, 2020) and A. Mummery et al. (2024). None of these mass estimates will significantly change our results.

[41] We note that the declining opacity of the envelope and/or a widening of the accretion funnel may further contribute to the increased X-ray luminosity.

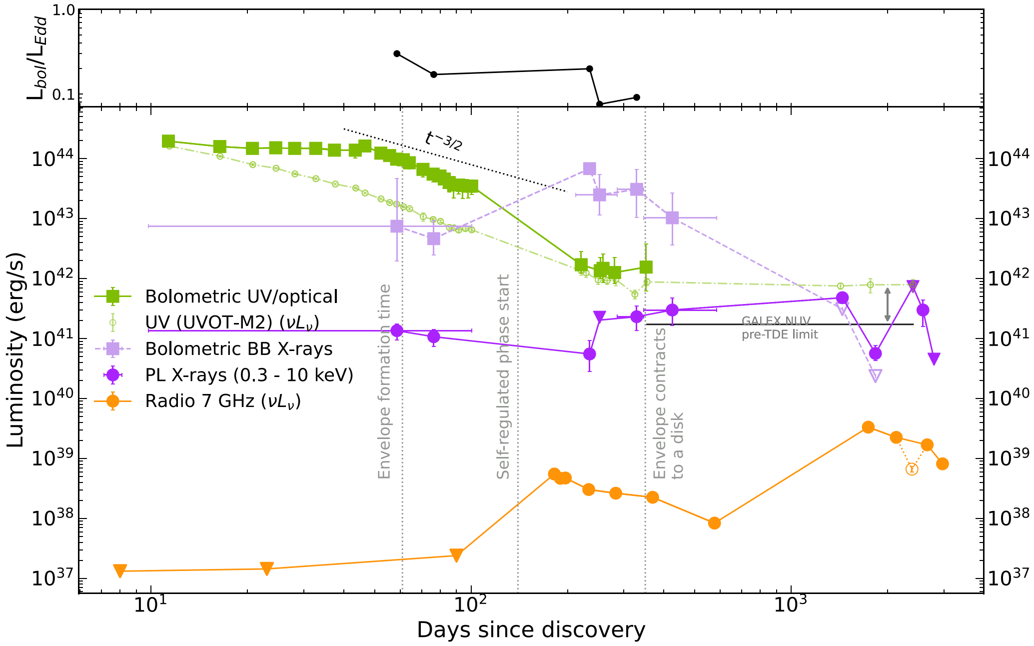

Figure 10. Bottom panel: multiband light-curve evolution of ASASSN-15oi from the time of discovery until ∼3000 days. The thermal emission is presented by squares, and the nonthermal emission is presented by circles. We plot the bolometric UVO emission in green. The UVO bolometric luminosity was calculated only for the epochs where enough spectral coverage was present across the UV and optical bands. At ∼3000 days post-disruption, the UVOT-m2 band luminosity (νL_ν at $\approx 1.5 \times 10^{15}$ Hz; small empty green circles) converges to a constant value, in contrast with continuing variability in the nonthermal X-rays. We show a dotted line with the trend $\propto t^{-3/2}$ predicted by the cooling envelope model for the optical luminosity. The thermal bolometric X-ray luminosity is shown with light-purple squares. The nonthermal power-law (PL) component of the X-rays in the energy range 0.3–10 keV is plotted with dark-purple circles. The nonthermal radio (νL_ν at $\nu \sim 7.5$ GHz) is plotted in orange, where the VLBA observation is plotted with an empty circle. Triangles indicate 3σ upper limits. Top panel: we plot the ratio of the total observed thermal bolometric luminosities $L_{X,\mathrm{BB,bol}} + L_{\mathrm{UVO,bol}}$ to L_{Edd} at $\lesssim$300 days. We note that it remains constant between $\delta t \approx 80$ and 230 days, with the rise in thermal X-ray emission compensating for the decline in the UVO emission.

efficiently accretion energy goes into the envelope versus being radiated, it can result in a flat light curve at all frequencies. We calculate the start time of this phase using the envelope-radius evolution Equation (27) in B. D. Metzger (2022) (also plotted with the gray dotted line in Figure 10). The observed $R_{\mathrm{ph}} \approx 8 \times 10^{13}$ cm during this phase matches the model's prediction (given by their Equation (37)). Y. Yao et al. (2023) similarly concluded that the evolution of optical/UV blackbody radius of ASASSN-15oi follows the trend predicted by B. D. Metzger (2022).

Another robust prediction of the cooling envelope model is for the total radiated luminosity to remain constant at the Eddington luminosity (L_{Edd}) while the envelope is contracting. In ASASSN-15oi, the total thermal bolometric luminosity (L_{bol}) indeed remains constant (from t_{fb} until the accretion peak at 230 days; top panel in Figure 10), although at sub-Eddington levels with $L_{\mathrm{bol}} \sim (0.2–0.3)L_{\mathrm{Edd}}$, which are consistent with other TDEs (e.g., T. Wevers et al. 2017). This can be reconciled with the model expectations (i.e., $L_{\mathrm{bol}} = L_{\mathrm{Edd}}$) if either most of the radiation is emitted at unobservable EUV wavelengths, and/or if the uncertainty in M_{BH} leads to an error in the calculation of L_{Edd}.

With this setup, the cooling envelope model predicts that the envelope would be completely accreted by $\delta t \sim 350$ days (their Equation (38); plotted with the gray dotted line in Figure 10). However, more realistically, the envelope might settle into an unobscured disk post X-ray peak, which can be modeled as a viscously spreading disk (e.g., J. K. Cannizzo et al. 1990; R. F. Shen & C. D. Matzner 2014; A. Mummery 2021). The resulting decrease in the inner disk temperature would account for the exponential decline in thermal X-rays observed after ∼350 days. As the disk spreads outward to larger radii, the emitting area increases while it cools, resulting in an almost constant emission that dominates the UV wavelengths (as these wavelengths lie near the Rayleigh–Jeans part of the disk spectrum). This is indeed the case in ASASSN-15oi, even at very late times ($\delta t \approx 2900$ days). Previous studies by S. van Velzen et al. (2019), A. Mummery & S. A. Balbus (2020), A. Mummery et al. (2024), and M. Guolo et al. (2024) also demonstrated that the late-time UV flattening observed in many other TDEs (e.g., ASASSN-14li, iPTF16fnl) is disk dominated and can be explained by longer ($\sim\mathcal{O}(10^3)$ days) viscous timescales at these larger radii.

Finally, while the predictions of the cooling envelope model and the subsequent evolution to a bare accretion disk match well with most of the thermal emission, certain other features observed in ASASSN-15oi remain unexplained. Particularly, the constant $L_{\mathrm{UVO,bol}}$ at $\delta t \lesssim t_{\mathrm{fb}} = 60$ days cannot be explained by the current analytical model. One can speculate that this flattening results from the complex processes taking place prior to/during the envelope formation, perhaps even due to stream–stream collisions as proposed by S. Gezari et al. (2017). Regarding the X-ray emission, the low S/N in the individual Swift-XRT observations during this period limits our understanding of the X-ray emission behavior at early times. We also currently lack an explanation for the constant blackbody temperature during the rise of the X-rays. A gradual rise in the accretion rate is expected to result in an increase in the temperature. This would be a problem if we were looking at a bare accretion disk at early times; however, as the geometry of the cooling envelope model is complex, we can expect an unconventional evolution of the thermal X-ray parameters depending on our observing angle.

4.2. Nonthermal Emission from ASASSN-15oi

Unlike the thermal emission, the spectral and temporal evolution of the nonthermal emission (see point Nos. 4, 5, and 6 in the overview list of Section 4) is extremely complex. In this Section, we briefly speculate on different physical processes/origins and additionally investigate whether the radio and nonthermal X-rays are physically related.

4.2.1. Possible Origin of the First Radio Flare

The first radio flare was analyzed in detail by A. Horesh et al. (2021a). Our results are broadly consistent with theirs. A particular feature determined here is the significant jump in the density estimates between the SEDs at $\delta t \approx 197$ days and 233 days. A. Horesh et al. (2021a) inferred similar jumps, and suggested that the outflow responsible for the first radio flare was unlikely to have been launched at the time of disruption and was likely delayed as a consequence of an accretion state transition. Alternatively, J. Zhuang et al. (2025) proposed that the first radio flare is powered by the interaction of an outflow with *three* different clouds present around the SMBH at ∼parsec scales. Their model explains the observed temporal evolution, although a close examination of their Figure 13 reveals discrepancies with the observed SEDs.

The energy and the velocity of the outflow that powers the initial radio flare are similar to those of other nonrelativistic TDEs (as seen in Figure 11). However, the time at which the first radio emission appears in ASASSN-15oi and the steep rise ($F \propto t^4$) from the prior nondetections are unusual compared to those of nonrelativistic TDEs with "prompt" emission (e.g., AT 2019dsg in Figure 5). Among commonly invoked scenarios that can also explain the somewhat higher kinetic energy in ASASSN-15oi (e.g., compared to the energy in ASASSN-14li as inferred by J. Krolik et al. 2016), we disfavor the scenario in which radio emission is powered by the interaction of a super-Eddington accretion-driven wind outflow with the ambient medium (K. D. Alexander et al. 2016; Y. Cendes et al. 2021a). This would require large accretion rates that, under the cooling envelope model, are not inferred in ASASSN-15oi until *after* the appearance of the first radio flare.

Instead, we find the case of a stream–stream CIO proposed by W. Lu & C. Bonnerot (2020) more likely. Episodic mass ejections during the envelope formation (at timescales $\lesssim t_{\rm fb} \sim 60$ days) are expected due to the repeated orbits of the self-colliding streams around the SMBH. This process creates a clumpy medium[42] with fast-moving material driving multiple shocks of varying energies (and possibly different microphysical parameters). For a significant amount (>20%) of initially unbound tidal debris moving at 0.01–0.1c, CIO is expected to dissipate 10^{49}–10^{52} erg kinetic energy over a diverse set of timescales. It is therefore possible that an outflow could decelerate over ∼100 days and power the first radio flare. The radio SEDs of, and velocity and energy derived from, the first flare (see Section 3.2) are consistent with this scenario, i.e., involving multiple outflows in an inhomogeneous medium. Detailed modeling for this scenario is left for future work.

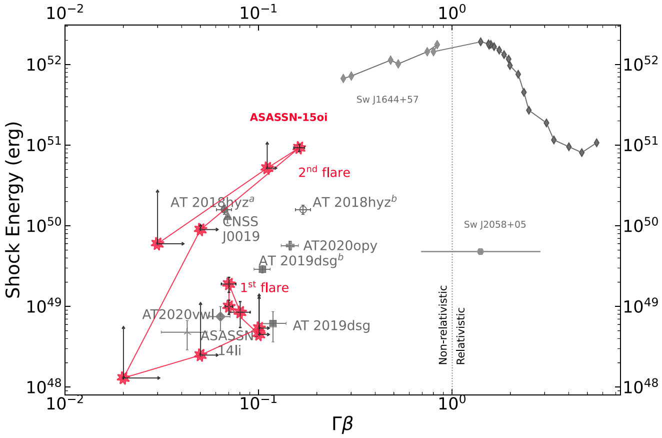

Figure 11. ASASSN-15oi in the context of other TDEs in the literature. The first radio flare of ASASSN-15oi shows energetics ($U_{\rm eq}$ from Section 3.2) similar to other nonrelativistic TDEs, while the second flare is the most energetic of the subset. For the purpose of comparison, we recalculate the energetics of other TDEs using the same R. A. Chevalier (1998) formulation that we used for ASASSN-15oi along with assuming equipartition. The two estimates for AT 2018hyz and AT 2019dsg are due to two different inferences of the outflow launch time. We also include some jetted TDEs that make up a very small fraction of all TDEs. Other references include: ASASSN-14li (K. D. Alexander et al. 2016); AT 2018hyz Y. Cendes et al. (2022); CNSS J0019+00 (M. M. Anderson et al. 2020); AT 2019dsg (Y. Cendes et al. 2021a); AT 2020opy (A. J. Goodwin et al. 2022); and AT 2020vwl (A. J. Goodwin et al. 2023).

4.2.2. Possible Origin of the Second Radio Flare

As seen in Figure 11, the outflow that powers the second radio flare carries substantially more energy than the one powering the first flare, suggesting distinct physical origins. In the recent study by Y. Sato et al. (2024), the authors modeled the two flares (with observations at $\delta t < 1500$ days) with a structured jet model consisting of a wide jet (responsible for the first flare) and a narrow jet (responsible for the second flare) with different shock microphysics, essentially the same scenario as the two distinct outflows that we propose here. Their conclusions are based solely on the temporal evolution. Their narrow jet (with $\theta_{\rm jet} \sim 6^\circ$ and $\theta_{\rm obs} \sim 70^\circ$) component that is responsible for the second radio flare carries kinetic energy ($E_{\rm k} \sim 10^{52}$ erg) similar to that of other TDEs in the literature. It is unclear, however, if their model can explain the observed spectral evolution.

Here, we propose that the second radio flare is powered by an outflow different from that of the first radio flare, and was likely launched when the accretion rate peaked (at $\gtrsim$200 days) in the context of the cooling envelope model discussed in Section 4.1. The outflow(s) may manifest as a relativistic jet or a quasi-spherical mildly relativistic wind interacting with the ambient medium. However, the details of the outflow powering the second radio flare are not well captured by simplified models, like those presented in Section 3, invoking the need for a more intricate model, perhaps similar to the one proposed for the first radio flare in the previous Section, but with a more powerful source that is launched significantly later after the disruption.

4.2.3. Possible Origin of the Nonthermal X-Rays

If the radio emission is indeed synchrotron emission, the latter may also extend to X-ray energies as well. We examine here if the nonthermal X-rays and first radio flare share the

---

[42] Fe II lines identified in ASASSN-15oi at $\delta t \sim 330$ days may also support the presence of optically thick clumps of gas (T. Wevers et al. 2021).

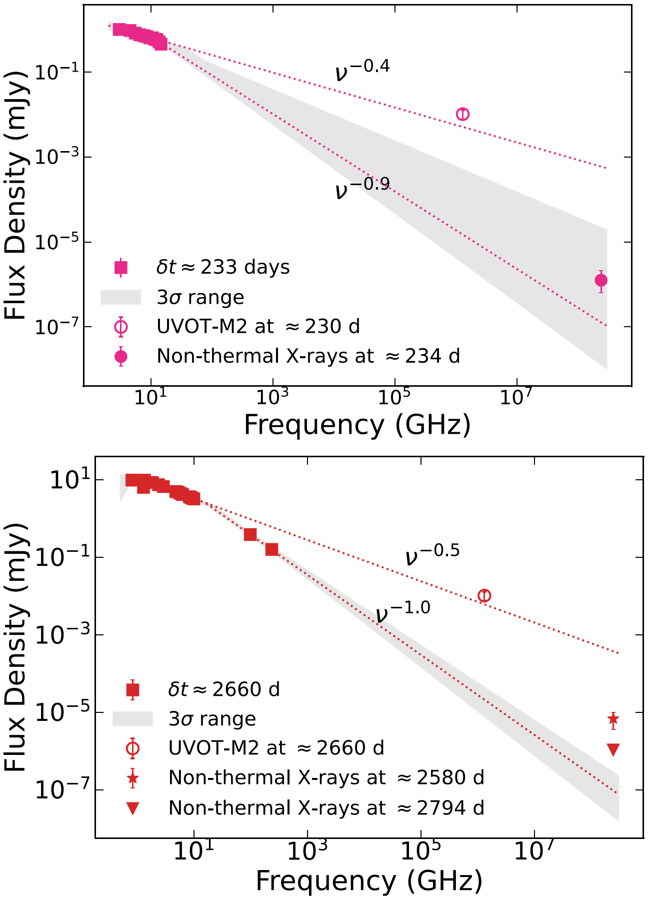

Figure 12. Broadband radio-to-X-ray SEDs of ASASSN-15oi associated with the radio flares at $\delta t \approx 233$ days (top, also coinciding with the peak of the X-rays) and $\delta t \approx 2660$ days, (bottom). Gray shaded areas are the 3σ ranges of the best-fitting spectra extrapolated from the radio observations to the X-rays. We also plot the median $\alpha_{\rm thin}$ and α_q segments as dotted lines. The open circles are UVOT-M2 observations. The plotted X-ray observations are the power-law component. At 233 days, the X-rays are consistent within 3σ of the extrapolation. However, the X-rays at 2580 days (closer in epoch to the radio observations) are clearly in excess. The X-ray upper limit at ≈2794 days, the next closest epoch to the radio, is also shown.

same synchrotron spectrum. As can be seen in the top panel of Figure 12, the nonthermal X-rays fall within the 3σ region of the extrapolated models[43] at $\delta t \approx 233$ days (the only epoch when both X-rays and radio were observed simultaneously). However, X-ray emission existed prior to the first radio flare, making them causally unrelated, unless the radio emission was absorbed at frequencies at least as high as 22 GHz for the first 180 days. An extremely large $n_e \sim 10^7\,{\rm cm}^{-3}$ is required if the source was synchrotron self-absorbed and its SSA spectrum were to peak at ∼22 GHz with $F_\nu \sim 0.06$ mJy at $\lesssim$180 days, which is unlikely. The higher densities found at ∼180 days in Section 3.2 could also potentially result in free–free absorption of the radio emission (K. W. Weiler et al. 2002). The free–free absorption optical depth is given by $\tau_{\rm FFA} \propto T_e^{-1.35}\nu^{-2.1}n_e^2 l$ (P. G. Mezger & A. P. Henderson 1967), where T_e is the electron temperature of the absorbing gas, and l is the optical path length along the line of sight. With the estimated n_e and R for $\delta t = 182$ days SED in Table 2, we find $\tau_{\rm FFA} < 1$ at ∼22 GHz. Therefore, if there was emission present at this frequency, it is unlikely to be affected by either synchrotron self-absorption or free–free absorption. Finally, the evolution of power-law X-rays and the radio emission is distinct, as can be seen in Figure 10, challenging the scenario of a shared source between the emission at the two wavelengths.

There is no strong evidence that the second radio flare and the late-time nonthermal X-ray emission share the same synchrotron spectrum because: (1) as seen in the lower panel of Figure 12, the $\delta t = 2580$ days X-rays (close to the epoch of the $\delta t = 2660$ days radio SED) are in excess of the extrapolation of the best-fitting radio model by $>3\sigma$. Therefore, the X-rays likely require a different mechanism. (2) In the latest observations, the steep decline in X-ray emission at $\delta t = 2790$ days precedes the steep decline in the radio emission at $\delta t = 2970$ days, also making them temporally inconsistent.

A common source for nonthermal X-rays in TDEs, independent of the synchrotron mechanism that powers the radio emission, is the inverse Compton scattering of the lower-energy photons from the accretion disk by an electron corona. Such coronae were identified in AT 2021ehb (Y. Yao et al. 2022), in AT 2018fyk (T. Wevers et al. 2021) and in a few others (M. Guolo et al. 2024), and can form or become strong during soft → hard state transitions (e.g., C. Done et al. 2007), similar to those in X-ray binary systems (XRBs). ASASSN-15oi does hint at state transitions of hard → soft → hard (top panel in Figure 2), and a direct comparison to the above studies suggests the presence of a corona at least at $\delta t \gtrsim 300$ days, after the soft → hard transition. The earlier hard → soft transition and the contemporaneous first radio flare in ASASSN-15oi also resemble behavior seen in XRBs, as previously noted by A. Horesh et al. (2021a). A similar evolution was observed in AT 2019azh, with a minor distinction that there the delayed radio flare, also occurring at ∼200 days, *followed* the hard → soft transition.

Assuming that the early- and late-time nonthermal X-rays share the same physical origin, the significant variability observed in the nonthermal X-rays at >1400 days may hint at changes in the disk (and/or corona). We note that the outer disk is likely stable, as the late-time UV emission originating in the outer regions (as discussed in Section 4.1) continues to plateau. And finally, the lag between the steep decline in the nonthermal X-rays and the steep decline in the radio at ∼3000 days can possibly be explained as a delay caused by the propagation of information from the inner regions of the disk to the radio-emitting components at larger distances from the SMBH (F. De Colle et al. 2012).

We briefly speculate on one possible scenario where all of these characteristics can be accounted for. We base our arguments on the premise that the physical processes governing accretion are universal around BHs independent of mass, and therefore, we draw inspiration from the phenomena observed in AGN and XRB systems. The scenario is that of a hybrid disk where (i) the inner disk is transitioning from a disk/corona system (possibly representative of the system at $\lesssim$1400 days) to an Advection-Dominated Accretion Flow (ADAF; e.g., R. Narayan & I. Yi 1994; B. Czerny et al. 2000); and (ii) the outer disk is likely a geometrically thin, optically thick stable standard disk. The transition in the inner regions can be triggered by a decrease in the mass-accretion rate below a critical value, as is often seen in XRBs in their low-hard state (e.g., A. A. Esin et al. 1997; M. van der Klis 2004). In XRBs/AGNs, this transition typically

---

[43] As discussed in Section 3.2.1, the break in the radio SED is likely not $\nu_{\rm cool}$. The real synchrotron cooling break can possibly lie anywhere between radio and X-rays and cause an even steeper spectral segment, which, when extrapolated to X-ray wavelengths, might make the observed X-rays appear in excess.

occurs at luminosity $\lesssim 10^{-2} L_{\rm Edd}$, which, for our SMBH mass, would be $\sim 10^{42}$ erg s^{-1}. Furthermore, at the interface between the inner ADAF and the outer regions, there may exist a narrow unstable zone where radiation pressure instabilities can induce the observed X-ray variability. The instabilities are driven on viscous timescales, which can be short depending on the size of this unstable zone, and can range from months to years (e.g., M. Sniegowska et al. 2020), similar to the timescale of the nonthermal X-ray variability we observe. As an example, a recent study by S. Veronese et al. (2024) attributed the long-term X-ray variability (at timescales of $\sim$10 yr) in Mrk 1018, a changing-look AGN, to a similar accretion flow transition in the inner disk.

There are other physical processes such as wind–torus interaction, proposed by G. Mou et al. (2021), that can produce variability in the X-ray emission at late times on approximately months to years timescales. In wind–torus interaction, the model-predicted luminosity, $\gtrsim 10^{41}$ erg s^{-1}, also matches the observed power-law X-ray luminosity. Such torii are usually present at $\sim$0.1 pc around AGNs. Although there are no infrared observations of ASASSN-15oi that could confirm a presence of a torus, , the presence of Fe II lines, as previously noted (see footnotes 42), may indicate the existence of optically thick clumps of gas. If this is indeed the case, that would imply that the early- and late-time nonthermal X-rays are powered by different sources.

We also want to emphasize that other TDEs have also shown late-time X-ray variability, albeit on shorter timescales ($\lesssim$days in, e.g., in AT 2018fyk, T. Wevers et al. 2021; and in AT 2019qiz, M. Nicholl et al. 2024). Due to our sparse temporal coverage, our observations are not sensitive to variability on $\sim$ day timescales. In addition, a simple Kolmogorov–Smirnov (K-S) test on our δt = 1833 XMM observation (Appendix B) revealed no evidence of a deviation from a constant count-rate on the timescale of $\sim$3 hr. Finally, we stress that our discussion here is only speculative, and we leave a more in-depth quantitative analysis to future work.

5. Summary and Conclusions

We have presented one of the most extensive data sets for a TDE, namely ASASSN-15oi, and our analysis thereof. ASASSN-15oi was observed across the electromagnetic spectrum using an array of telescopes including the VLA, VLBA, MeerKAT, ATCA, ALMA, Swift-UVOT, Swift-XRT, and XMM-Newton. We rereduced and reanalyzed the previously reported UV and X-ray observations here to provide a homogeneous data set. We have also presented new observations obtained through our coordinated multiwavelength campaigns, particularly following the occurrence of the second radio flare, at $\delta t > 1400$ days until $\sim$8 yr. We note that ASASSN-15oi was the first TDE observed to have multiple radio flares, and highlights the importance of long-term monitoring of TDEs. We study the emission at different wavelengths individually, but also investigate any physical connection between them within the framework of existing models. We summarize our findings below.

We divide the observed emission of ASASSN-15oi into thermal and nonthermal emission. We treat the emission dominating the optical and UV wavelengths and the blackbody component of the X-rays as thermal. We find that the *cooling envelope* model proposed by B. D. Metzger (2022) can explain the evolution of the thermal emission in ASASSN-15oi extremely well, as presented in Section 4.1. In this model, the radiative cooling of a quasi-spherical envelope formed after the stellar disruption drives the optical/UV emission, different from the interpretations of typical TDEs where the optical/UV emission is either produced in stream–stream collisions, or via reprocessing of the X-rays by the surrounding material. This model naturally explains the delayed rise of the thermal X-rays, as more and more material gets accreted onto the SMBH. The envelope then transforms into a bare accretion disk that spreads outward on long viscous timescales, explaining the eventual decline in the thermal X-rays in the inner regions and the late-time persisting UV plateau emitting from the outer disk.

Unlike the thermal emission, qualitatively explaining the nonthermal emission, i.e., the power-law component of the X-rays and the radio emission, is more challenging. In Section 4.2, we posited the first ($\delta t \lesssim 600$ days) and second ($\delta t \gtrsim 1400$ days) radio flares to have distinct origins. A simplified approach of either a spherical blastwave or an ultrarelativistic off-axis top-hat jet interacting with the ambient medium alone cannot explain the observed spectral and temporal radio evolution without requiring unphysical conditions. Therefore, to account for the spectral variations and the sharp jumps in the physical parameters of the system (as derived in Section 3.2) within the first radio flare, we invoke a more complex system with multiple outflows launched in an inhomogeneous medium such as that produced by stream–stream collision-induced outflows (discussed in Section 4.2) during the *envelope* formation. The second radio flare is possibly produced by a similarly complex, but more powerful outflow launched as a result of the accretion rate reaching its peak in the context of the cooling envelope model. Finally, the nonthermal X-rays seem to be produced by a different mechanism, or particle population, than that producing the radio synchrotron emission. In Section 4.2.3, we briefly discuss the possible near-disk origin of the nonthermal X-rays. We emphasize that this is purely speculative, and future monitoring of ASASSN-15oi and developing more sophisticated models will be crucial to confirm the origin of its late-time emission.

In conclusion, the multiwavelength observations of ASASSN-15oi reveal a complex picture of TDEs and their long-term evolution. The detailed data set allows us to probe the different emission mechanisms at various frequencies and phases in the "life" of a TDE. Our study emphasizes the importance of late-time observations across the electromagnetic spectrum for better understanding of TDEs. The late-time monitoring may help address the "missing energy" problem in TDEs (as detailed in W. Lu & P. Kumar 2018) where the observed radiated energy in most TDEs is $\approx 10^{51}$ erg (e.g., B. Mockler & E. Ramirez-Ruiz 2021), which falls short of the expected 10^{52}–10^{53} erg. Since its discovery, ASASSN-15oi has radiated 2×10^{51} erg in X-rays, UV, and optical, with the first radio flare contributing an additional a few $\times 10^{49}$ erg of kinetic energy to the total energy budget. We further find that the second radio flare carries an energy $\gtrsim 10^{51}$ erg (in Section 3.2), potentially more if a jet is involved. This suggests that the kinetic energy of the outflows is a substantial fraction of the overall energy budget and that multiple delayed radio flares could be more common in TDEs (as indeed was found in Y. Cendes et al. 2024) harboring the energy deficit. Thus, long-term monitoring of TDEs is crucial, not only to understand their complexities, but also to uncover hidden or delayed emission sources that may resolve the missing energy problem. Exploring the late-time phase in TDEs has only been a recent occurrence, and ASASSN-15oi has clearly demonstrated its importance, but also a need for more complex and nuanced models to incorporate the diverse and evolving nature of TDEs.

Acknowledgments

The authors thank the anonymous referee for providing a constructive review, which helped in robustly verifying our results and the overall improvement of the manuscript. The authors thank Clement Bonnerot, Damiano Caprioli, Brian Metzger, and Juergen Ott from the NRAO helpdesk for helpful discussions. We acknowledge the use of public data from the Swift data archive. XMM-Newton is an ESA science mission with instruments and contributions directly funded by ESA Member States and NASA. The National Radio Astronomy Observatory is a facility of the National Science Foundation operated under cooperative agreement by Associated Universities, Inc. The MeerKAT telescope is operated by the South African Radio Astronomy Observatory, which is a facility of the National Research Foundation, an agency of the Department of Science and Innovation. The Australia Telescope Compact Array is part of the Australia Telescope National Facility,[44] which is funded by the Australian Government for operation as a National Facility managed by CSIRO. This paper makes use of the following ALMA data: ADS/JAO.ALMA#2019.1.01166.T. ALMA is a partnership of ESO (representing its member states), NSF (USA), and NINS (Japan), together with NRC (Canada), NSTC and ASIAA (Taiwan), and KASI (Republic of Korea), in cooperation with the Republic of Chile. The Joint ALMA Observatory is operated by ESO, AUI/NRAO, and NAOJ.

A.H. was supported by a Future Investigators in NASA Earth and Space Science and Technology (FINESST) award No. 80NSSC19K1422 during the initial stages of this project. A.H. also acknowledges support from the Carlsberg Foundation Fellowship Programme by Carlsbergfondet and from VILLUM FONDEN research grants VIL16599 and VIL54489. K.D.A. and C.T.C. acknowledge support provided by the National Science Foundation through award SOSPA9-007 from the NRAO and award AST-2307668. R.M. acknowledges support by the National Science Foundation under award Nos. AST-2221789 and AST-2224255. The TReX team at UC Berkeley is partially funded by the Heising-Simons Foundation under grant 2021-3248 (PI: Margutti). M.B. is grateful for computing and office support from York University, Canada. E.R-R. acknowledges support from the Heising-Simons Foundation, NSF grants AST-2150255 and AST-2307710. A.H. is grateful for the support by the United States–Israel Binational Science Foundation (BSF grant 2020203) and by the Sir Zelman Cowen Universities Fund. This research was supported by the ISRAEL SCIENCE FOUNDATION (grant No. 1679/23). A.H. also acknowledges partial support by the NSF grant PHY-2309135 to the Kavli Institute for Theoretical Physics (KITP).

Appendix A
Broadband Observations of ASASSN-15oi

Here we provide optical and UV photometry (Table A1), X-ray fluxes and other parameters derived from spectral modeling (Table A2), and radio flux density measurements of ASASSN-15oi (Table A3).

Table A1
Swift-UVOT Photometry

Epoch (MJD)	δt (days)	Filter	Magnitude	Error	Epoch (MJD)	δt (days)	Filter	Magnitude	Error
57259.41	11.41	*v*	15.974	0.051	57336.40	88.4	uvw1	19.039	0.099
57264.42	16.42	*v*	16.298	0.056	57339.43	91.43	uvw1	18.991	0.101
57270.71	22.71	*v*	16.664	0.057	57342.10	94.10	uvw1	19.059	0.124
57276.13	28.13	*v*	16.781	0.070	57345.79	97.79	uvw1	19.261	0.150
57280.72	32.72	*v*	16.831	0.071	57348.41	100.41	uvw1	19.319	0.113
57288.50	40.5	*v*	16.793	0.073	57468.80	220.80	uvw1	20.265	0.197
57300.57	52.57	*v*	16.953	0.054	57484.95	236.95	uvw1	20.532	0.153
57318.89	70.89	*v*	17.061	0.059	57508.58	260.58	uvw1	20.416	0.103
57340.96	92.96	*v*	17.066	0.061	57527.29	279.29	uvw1	20.450	0.113
57501.11	253.11	*v*	17.016	0.064	57572.84	324.84	uvw1	20.596	0.127
57572.85	324.85	*v*	17.135	0.064	57602.41	354.41	uvw1	20.714	0.148
57602.42	354.42	*v*	17.195	0.074	58674.29	1426.29	uvw1	20.633	0.090
58674.29	1426.29	*v*	17.139	0.041	59020.30	1772.30	uvw1	20.684	0.203
59649.93	2401.93	*v*	17.234	0.088	59649.93	2401.93	uvw1	20.698	0.200
59784.74	2536.74	*v*	17.109	0.105	59828.39	2580.39	uvw1	21.003	0.235
57259.40	11.40	*b*	15.995	0.039	57259.41	11.41	uvm2	15.590	0.041
57259.42	16.42	*b*	16.374	0.042	57259.43	16.43	uvm2	16.017	0.042
57268.75	20.75	*b*	16.542	0.043	57268.79	20.79	uvm2	16.366	0.052
57272.57	24.57	*b*	16.808	0.047	57272.58	24.58	uvm2	16.516	0.044
57276.12	28.12	*b*	16.919	0.049	57276.13	28.13	uvm2	16.750	0.046
57280.71	32.71	*b*	17.046	0.051	57280.72	32.72	uvm2	16.951	0.047
57285.64	37.64	*b*	17.147	0.065	57285.64	37.64	uvm2	17.174	0.045
57291.48	43.48	*b*	17.241	0.067	57291.59	43.59	uvm2	17.340	0.054
57294.61	46.61	*b*	17.358	0.074	57294.62	46.62	uvm2	17.545	0.047
57300.26	52.26	*b*	17.355	0.071	57300.27	52.27	uvm2	17.793	0.048
57303.66	55.66	*b*	17.406	0.081	57303.66	55.66	uvm2	17.945	0.053

---

[44] https://ror.org/05qajvd42

Table A1
(Continued)

Epoch (MJD)	δt (days)	Filter	Magnitude	Error
57306.52	58.52	*b*	17.345	0.075
57309.48	61.48	*b*	17.462	0.080
57312.20	64.20	*b*	17.349	0.086
57318.77	70.77	*b*	17.573	0.085
57324.08	76.08	*b*	17.630	0.123
57328.14	80.14	*b*	17.644	0.093
57333.48	85.48	*b*	17.634	0.100
57336.40	88.40	*b*	17.649	0.116
57340.73	92.73	*b*	17.687	0.089
57347.12	99.12	*b*	17.817	0.098
57501.10	253.10	*b*	17.914	0.065
57572.84	324.84	*b*	17.907	0.061
57602.41	354.41	*b*	17.861	0.064
58674.29	1426.29	*b*	17.931	0.041
59649.93	2401.93	*b*	17.890	0.077
59784.74	2536.74	*b*	17.803	0.095
57259.40	11.40	*u*	15.972	0.037
57259.41	16.41	*u*	16.434	0.040
57268.75	20.75	*u*	16.728	0.041
57272.57	24.57	*u*	16.964	0.044
57276.12	28.12	*u*	17.199	0.047
57280.71	32.71	*u*	17.460	0.050
57285.64	37.64	*u*	17.572	0.062
57291.48	43.48	*u*	17.697	0.065
57294.61	46.61	*u*	17.933	0.075
57300.26	52.26	*u*	18.080	0.078
57303.65	55.65	*u*	18.048	0.084
57306.52	58.52	*u*	18.165	0.085
57309.48	61.48	*u*	18.283	0.090
57312.20	64.20	*u*	18.331	0.109
57318.77	70.77	*u*	18.338	0.093
57326.21	78.21	*u*	18.413	0.084
57335.04	87.04	*u*	18.452	0.086
57340.73	92.73	*u*	18.731	0.113
57347.11	99.11	*u*	18.787	0.119
57460.27	212.27	*u*	19.321	0.063
57501.10	253.10	*u*	19.327	0.104
57572.84	324.84	*u*	19.264	0.093
57602.41	354.41	*u*	19.247	0.100
58674.29	1426.29	*u*	19.264	0.057
59649.93	2401.93	*u*	19.246	0.119
59784.73	2536.73	*u*	19.074	0.142
57259.40	11.40	uvw1	15.770	0.040
57259.41	16.41	uvw1	16.153	0.041
57268.75	20.75	uvw1	16.459	0.042
57272.57	24.57	uvw1	16.678	0.044
57276.12	28.12	uvw1	16.985	0.046
57280.71	32.71	uvw1	17.207	0.047
57285.64	37.64	uvw1	17.419	0.050
57291.48	43.48	uvw1	17.667	0.053
57294.61	46.61	uvw1	17.782	0.056
57297.05	49.05	uvw1	18.047	0.078
57300.26	52.26	uvw1	18.059	0.059
57303.65	55.65	uvw1	18.239	0.069
57306.52	58.52	uvw1	18.313	0.067
57309.47	61.47	uvw1	18.337	0.066
57312.20	64.20	uvw1	18.496	0.076
57318.77	70.77	uvw1	18.590	0.072
57324.08	76.08	uvw1	18.861	0.104
57328.14	80.14	uvw1	18.967	0.088
57333.48	85.48	uvw1	18.992	0.093
57306.52	58.52	uvm2	18.014	0.052
57309.48	61.48	uvm2	18.122	0.054
57312.20	64.20	uvm2	18.203	0.056
57318.87	70.87	uvm2	18.537	0.176
57324.09	76.09	uvm2	18.653	0.071
57328.17	80.17	uvm2	18.730	0.066
57333.52	85.52	uvm2	18.984	0.077
57336.41	88.41	uvm2	19.000	0.072
57339.44	91.44	uvm2	19.091	0.077
57343.93	95.93	uvm2	19.031	0.085
57348.42	100.42	uvm2	19.084	0.077
57468.80	220.80	uvm2	20.788	0.175
57476.65	228.65	uvm2	20.874	0.178
57497.32	249.32	uvm2	21.166	0.180
57514.00	266	uvm2	21.197	0.153
57531.25	283.25	uvm2	21.153	0.234
57572.85	324.85	uvm2	21.767	0.185
57602.42	354.42	uvm2	21.251	0.154
58674.29	1426.29	uvm2	21.423	0.126
59016.54	1768.54	uvm2	21.373	0.290
59649.93	2401.93	uvm2	21.368	0.247
59828.39	2580.39	uvm2	21.488	0.313
57257.83	9.83	uvw2	15.957	0.039
57259.40	11.40	uvw2	15.986	0.039
57259.42	16.42	uvw2	16.300	0.040
57268.75	20.75	uvw2	16.455	0.043
57272.57	24.57	uvw2	16.656	0.041
57276.12	28.12	uvw2	16.842	0.041
57280.72	32.72	uvw2	17.044	0.042
57285.64	37.64	uvw2	17.157	0.044
57291.49	43.49	uvw2	17.312	0.046
57294.62	46.62	uvw2	17.331	0.045
57300.27	52.27	uvw2	17.550	0.046
57303.66	55.66	uvw2	17.577	0.048
57306.52	58.52	uvw2	17.756	0.049
57309.48	61.48	uvw2	17.815	0.049
57312.20	64.20	uvw2	17.933	0.052
57318.77	70.77	uvw2	18.168	0.053
57324.08	76.08	uvw2	18.254	0.064
57328.14	80.14	uvw2	18.342	0.058
57333.48	85.48	uvw2	18.548	0.066
57336.41	88.41	uvw2	18.545	0.062
57339.43	91.43	uvw2	18.606	0.066
57342.10	94.10	uvw2	18.603	0.077
57345.79	97.79	uvw2	18.652	0.083
57348.41	100.41	uvw2	18.782	0.066
57468.80	220.80	uvw2	20.830	0.191
57476.65	228.65	uvw2	20.702	0.165
57493.43	245.43	uvw2	20.916	0.207
57501.27	253.27	uvw2	21.062	0.175
57506.29	258.29	uvw2	21.073	0.199
57515.12	267.12	uvw2	21.112	0.243
57521.44	273.44	uvw2	21.178	0.215
57530.88	282.88	uvw2	21.300	0.218
57585.00	337	uvw2	21.259	0.105
57839.52	591.52	uvw2	21.406	0.137
58674.29	1426.29	uvw2	21.521	0.102
59016.54	1768.54	uvw2	21.468	0.246
59649.93	2401.93	uvw2	21.464	0.197
59828.39	2580.39	uvw2	21.289	0.215

Note. All of the magnitudes and the corresponding errors are reported in the AB magnitude system, and are corrected for Galactic extinction.

Table A2
Best-fitting Results from the Time-resolved X-Ray Spectral Analysis of ASASSN-15oi Using Swift-XRT (Upper Part) and XMM-Newton (Lower Part)

δt[a]	Exposure	PL		BB			Total	Source
		Γ_X	Unabsorbed Flux ($\times 10^{-14}$ erg cm^{-2} s^{-1})	$kT_{\rm BB}$	Unabsorbed Flux ($\times 10^{-13}$ erg cm^{-2} s^{-1})	$R_{\rm BB}$	Absorbed Flux ($\times 10^{-14}$ erg cm^{-2} s^{-1})	
(days)	(ks)			($\times 10^{-2}$ keV)		($\times 10^{12}$ cm)		
				Swift-XRT				
58.6	61.7	$1.7^{+0.5}_{-0.5}$	$2.4^{+0.7}_{-0.7}$	$4.5^{+0.5}_{-0.6}$	$1.3^{+0.2}_{-0.2}$	$0.4^{+0.4}_{-0.1}$	7^{+1}_{-1}	This Work
252.1	31	2.0	<3.6	$4.9^{+0.3}_{-0.3}$	$6.5^{+0.7}_{-0.6}$	$0.6^{+0.2}_{-0.1}$	29^{+1}_{-6}	This Work
329.0	11.7	}2.0	$4.1^{+2.1}_{-1.7}$	}$5.2^{+0.4}_{-0.4}$	$8.9^{+1.2}_{-1.0}$	$0.6^{+0.2}_{-0.2}$	44^{+5}_{-5}	This Work
425.1	6.1		$5.3^{+3.1}_{-2.4}$		$2.9^{+0.9}_{-0.7}$	$0.3^{+0.1}_{-0.1}$	18^{+5}_{-3}	This Work
1444.9	25.3	$2.3^{+0.3}_{-0.3}$	$8.5^{+1.4}_{-1.5}$	5.2	<0.6	–	–	This Work
2401	7.2	2	<17	–	–	–	–	This Work
2580	7.0	2	$5.3^{+2.5}_{-2.5}$	–	–	–	–	This Work
				XMM-Newton [b]				
76.4	10.3	$2.5^{+0.8}_{-0.8}$	–[c]	$4.7^{+0.2}_{-0.2}$	1.6	0.4	7	S. Gezari et al. (2017)
76.4	12.4	$1.7^{+1.0}_{-0.8}$	$2.3^{+0.8}_{-0.8}$	6.2^{+6}_{-6}	$1.2^{+0.5}_{-0.5}$	$0.5^{+0.6}_{-0.6}$	–	T. W. S. Holoien et al. (2018)
76.4	9.7	$1.5^{+0.5}_{-0.4}$	$1.9^{+0.6}_{-0.6}$	$5.1^{+0.3}_{-0.3}$	$1.3^{+0.1}_{-0.1}$	$0.2^{+0.1}_{-0.1}$	8^{+1}_{-1}	This Work
234.5	12.0	$3.3^{+1.3}_{-1.3}$	–	$4.2^{+0.1}_{-0.1}$	18	2.1	37	S. Gezari et al. (2017)
234.5	14.0	$4.8^{+2.6}_{-1.2}$	$1.5^{+0.8}_{-0.8}$	5.3^{+2}_{-2}	$3.2^{+0.9}_{-1.0}$	$1.1^{+0.8}_{-0.8}$	–	T. W. S. Holoien et al. (2018)
234.5	10.9	$3.1^{+1.2}_{-0.9}$	$0.9^{+0.7}_{-0.5}$	$4.2^{+0.1}_{-0.1}$	$8.9^{+0.2}_{-0.2}$	$1.3^{+0.1}_{-0.1}$	38^{+1}_{-1}	This Work
1833	12.5	$2.0^{+0.3}_{-0.3}$	$1.0^{+0.4}_{-0.2}$	5.2	$<4.2 \times 10^{-2}$	–	–	This Work
2794	19.7	2	<0.8	–	–	–	–	This Work

Notes. The data require two components of emission using a spectral model of the form `tbabs*(cflux*pow+cflux*bbody)` within `XSPEC`. We adopted $N_{\rm H,gal} = 5.59 \times 10^{20}$ cm^{-2}, $N_{\rm H,int} = 0$ cm^{-2}, and redshift $z = 0.0484$. XMM-Newton (Swift-XRT) observations are fitted in the 0.2–12 keV (0.3–10 keV) energy range. Fluxes are reported in the 0.3–10 keV energy range, uncertainties are reported at the 68% confidence (1σ) level, and upper limits are reported at the 3σ confidence level. Γ_X is the power-law photon index, and $kT_{\rm BB}$ is the observed blackbody temperature in kiloelectronvolt units. For XMM-Newton, we report the EPIC-pn exposure times after removal of the time intervals affected by high background.

[a] For Swift-XRT, we list the mean time of arrival of the photons. From top to bottom, the interval of times of extraction of the spectra are 9.8–100.5 days, 212.2–285.5 days, 285.5–346.4 days, 346.4–585.7 days, 1394.9–1774.2 days, 2401 days, and 2540–2620 days.

[b] For XMM, we provide the numbers reported in the earlier works of S. Gezari et al. (2017) and T. W. S. Holoien et al. (2018) for the purpose of comparison.

[c] The columns with no values (–) were not reported in the previously published works. The empty columns in the last XMM and XRT observations where we report the values from this work are because of the unconstrained nature of the BB component at these epochs.

Table A3
Radio Observations of the TDE ASASSN-15oi

Date	Observatory	Project	ν (GHz)	F_ν (mJy)	Source
$\delta t = 8$ days					
2015 Aug 22	VLA	16A-422	6.1	<0.03	A. Horesh et al. (2021a)
		(PI: Horesh)	7.1	<0.03	
			22	<0.06	
$\delta t = 23$ days					
2015 Sep 6	VLA	16A-422	6.1	<0.04	A. Horesh et al. (2021a)
		(PI: Horesh)	7.1	<0.04	
			22	<0.07	
$\delta t = 90$ days					
2015 Nov 12	VLA	16A-422	6.1	<0.06	
		(PI: Horesh)	7.1	<0.06	
			22	<0.03	
$\delta t = 182$ days					

Table A3
(Continued)

Date	Observatory	Project	ν (GHz)	F_ν (mJy)	Source
2016 Feb 12	VLA	16A-422 (PI: Horesh)	4.8	1.11 ± 0.06	A. Horesh et al. (2021a)
			7.4	1.32 ± 0.07	
			19	0.83 ± 0.05	
			21	0.81 ± 0.04	
			23	0.64 ± 0.04	
			25	0.59 ± 0.04	
δt = 190 days					
2016 Feb 20	VLA	16A-422 (PI: Horesh)	3	0.55 ± 0.03	A. Horesh et al. (2021a)
			4.8	0.89 ± 0.05	
			7.4	1.12 ± 0.06	
			9	1.20 ± 0.06	
			11	1.07 ± 0.06	
			13	1.10 ± 0.06	
			15	0.93 ± 0.05	
			17	0.78 ± 0.04	
			19	0.72 ± 0.04	
			21	0.57 ± 0.03	
			23	0.49 ± 0.03	
			25	0.45 ± 0.03	
δt = 197 days					
2016 Feb 27	VLA	16A-422 (PI: Horesh)	3	0.50 ± 0.03	A. Horesh et al. (2021a)
			4.5	0.69 ± 0.04	
			5.5	0.88 ± 0.04	
			6.5	1.04 ± 0.05	
			7.5	1.12 ± 0.06	
			9	1.07 ± 0.06	
			11	1.03 ± 0.05	
			13	0.93 ± 0.05	
			15	0.79 ± 0.04	
			17	0.70 ± 0.04	
			19	0.72 ± 0.04	
			21	0.69 ± 0.04	
			23	0.53 ± 0.03	
			25	0.43 ± 0.03	
δt = 233 days					
2016 Apr 3	VLA	16A-422 (PI: Horesh)	3	1.01 ± 0.06	A. Horesh et al. (2021a)
			4.5	0.95 ± 0.05	
			5.5	0.82 ± 0.04	
			6.5	0.76 ± 0.04	
			7.5	0.72 ± 0.04	
			8.5	0.69 ± 0.04	
			9.5	0.64 ± 0.03	
			10.5	0.64 ± 0.03	
			11.5	0.59 ± 0.03	
			12.5	0.58 ± 0.03	
			13.5	0.51 ± 0.03	
			14.5	0.45 ± 0.03	
δt = 283 days					
2016 May 23	VLA	16A-422 (PI: Horesh)	3	1.03 ± 0.06	A. Horesh et al. (2021a)
			5	0.85 ± 0.04	
			7	0.67 ± 0.04	
			9	0.58 ± 0.03	
			11	0.52 ± 0.03	
			13	0.43 ± 0.02	
			15	0.36 ± 0.02	
			17	0.32 ± 0.02	
δt = 369 days					

Table A3

(Continued)

Date	Observatory	Project	ν (GHz)	F_ν (mJy)	Source
2016 Aug 17	VLA	16A-422	3	0.69 ± 0.04	A. Horesh et al. (2021a)
		(PI: Horesh)	5	0.62 ± 0.04	
			7	0.57 ± 0.03	
			9	0.55 ± 0.03	
δt = 576 days					
2017 Mar 12	VLA	16A-422	3	0.31 ± 0.07	A. Horesh et al. (2021a)
		(PI: Horesh)	5	0.23 ± 0.03	
			7	0.21 ± 0.02	
			9	0.20 ± 0.02	
δt = 1417 days					
2019 Jul 1	VLA	VLASS	3	9.5 ± 0.5	
δt = 1741 days					
2020 May 20	VLA	20A-492	1.3	9.8 ± 0.5	This Work
		(PI: Alexander)	1.8	10.8 ± 0.6	
			2.5	10.1 ± 0.5	
			3.5	9.6 ± 0.5	
			5	9.3 ± 0.5	
			7	8.4 ± 0.4	
			9	7.3 ± 0.3	
			11	6.3 ± 0.4	
δt = 2129 days					
2021 Jun 8	VLA	21A-303	1.2	11.3 ± 0.6	This Work
		(PI: Hajela)	1.6	11.2 ± 0.6	
			1.9	10.8 ± 0.6	
			2.3	9.9 ± 0.6	
			2.8	9.2 ± 0.5	
			3.2	8.6 ± 0.4	
			3.8	7.9 ± 0.4	
			4.5	7.1 ± 0.4	
			5.5	6.2 ± 0.3	
			6.5	5.4 ± 0.3	
			8.5	4.7 ± 0.2	
			9.5	4.4 ± 0.2	
			10.5	4.1 ± 0.2	
			11.5	3.8 ± 0.2	
δt = 2384 days					
2022 Feb 22	VLBI	BH 238	8.3	1.4 ± 0.3	This Work
		(PI: Hajela)			
δt = 2660 days					
2023 Jan 5	MeerKAT	DDD-20220414-YC-01	0.8	9.8 ± 0.5	This Work
2022 Dec 9	MeerKAT	SCI-20220822-YC-01	1.3	6.4 ± 0.3	
		(PI: Cendes)			
2022 Sep 30	ATCA	C3325	1.3	9.7 ± 1.3	
		(PI: Alexander)	1.8	8.5 ± 0.9	
			2.4	7.4 ± 0.8	
			2.9	6.7 ± 0.7	
			4.7	4.9 ± 0.5	
			5.2	4.8 ± 0.5	
			5.8	4.4 ± 0.4	
			6.3	4.2 ± 0.4	
			8.2	3.6 ± 0.4	
			8.7	3.5 ± 0.3	
			9.3	3.4 ± 0.3	
			9.9	3.2 ± 0.4	

Table A3
(Continued)

Date	Observatory	Project	ν (GHz)	F_ν (mJy)	Source
2022 Sep 29	ALMA	2019.1.01166.T	97.5	0.38 ± 0.02	
		(PI: Alexander)	233	0.16 ± 0.02	
$\delta t = 2970$ days					
2023 Oct 1	VLA	23A-241	1.2	4.1 ± 0.2	This Work
		(PI: Cendes)	1.5	3.7 ± 0.2	
			1.9	3.5 ± 0.2	
			2.3	3.5 ± 0.2	
			2.9	3.1 ± 0.2	
			3.6	3.1 ± 0.2	
			4.5	2.6 ± 0.1	
			5.5	2.4 ± 0.1	
			6.5	2.1 ± 0.1	
			7.5	1.9 ± 0.1	
			8.5	1.7 ± 0.1	
			9.5	1.5 ± 0.1	
			10.5	1.4 ± 0.1	
			11.5	1.4 ± 0.1	

Note. The VLA observations at $\delta t < 600$ days were reported in A. Horesh et al. (2021a); however, we include the contribution for systematic uncertainties here that accounts for the inaccuracies in the flux density calibration. A 5%, 10%, 3%, and 6% systematic uncertainty is added in quadrature to the uncertainties of all of the flux densities measured by the VLA, ATCA, and ALMA Band 3 and ALMA Band 6, respectively. For MeerKAT, the reported uncertainties are a combination of 5% systematic, image background rms, and the standard deviation over three methods ((i) peak brightness (interpolated between pixels); (ii) fit beam-shaped Gaussian + zero level; and (iii) total over a 10 pixel region, corrected for the fitted zero level from previous fit) of extracting the flux density—all added in quadrature. The upper limits are 3 × the image background rms values.

Appendix B
Search for Short-term Temporal Variability in the $\delta t = 1833$ day XMM Observation

We conducted a statistical test to assess the temporal variability of the X-ray emission from ASASSN-15oi within the latest $\delta t = 1833$ days XMM observation that is dominated by the power-law component and in which the source is significantly detected. We performed a Kolmogorov–Smirnov (K-S) test to compare the cumulative distribution function (CDF) of the observed photon arrival times with the expected uniform distribution under the null hypothesis of a constant count-rate. The K-S test makes no assumption on the binning of the data, and is sensitive to *any* deviation from the null hypothesis at any time during the observation.

To construct the observed CDF, we accounted for observational gaps in the data by incorporating good time interval information and applying fractional exposure corrections. This information was retrieved from the corrected time series generated by the XMM-SAS task, `epiclccorr`, which accounts for detector dead time and other variations in instrument efficiency. We then adjusted or remapped the photon arrival times such that they form a continuous timeline spanning the net exposure time of the observation ($t_{\rm expo} = 12.5$ ks). We calculate the observed test statistic ($TS_{\rm obs}$) as the maximum deviation of the observed CDF from the expected CDF for a constant count-rate source.

To evaluate the statistical significance of any deviations, we generated 1000 independent simulations of a constant count-rate source. In each simulation, the total observed photons were randomly distributed uniformly over the time interval [0, $t_{\rm exp}$]. For each simulation, the test statistic ($TS_{\rm sim}$) was calculated as the maximum deviation of the simulated CDF between the simulated CDF and the expected uniform CDF. Our test yielded a high p-value with only a very small fraction of simulated data sets with $TS_{\rm sim} \geqslant TS_{\rm obs}$. This suggests that the observed photon arrival times are consistent with a constant count-rate source, with any apparent deviations likely due to random fluctuations. The consistency of the observed CDF with the expected CDF can also be seen in Figure B1.

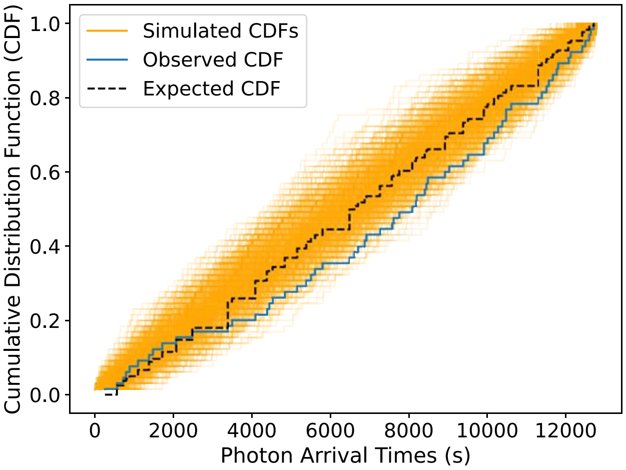

Figure B1. Comparison of cumulative distribution functions (CDFs) of the observed (in blue), expected (in black), and the simulated (in orange) data sets. The observed CDF closely follows the CDF of the expected constant count-rate CDF.

Appendix C
Radio Spectral Fitting and the Model Selection Criteria

In Appendices C.1 and C.2, we explain the fitting process in detail, along with our underlying assumptions. In Appendix C.3, we give details of our model selection criteria.

C.1. Fit of SEDs Associated with the First Radio Flare

We first fit the $\delta t = 182$ day, 190 day, and 197 day SEDs with Equation (2), assuming values of $s_1 = -0.3$ and a sharper $s_2 = -0.003$. We set $\alpha_{\rm thick,\,thin}$ as free parameters for the 190 and 197 days SEDs, resulting in $\alpha_{\rm thick} \sim +1$. We fix $\alpha_{\rm thick}$ at $+1$ for the 182 day SED, at which there are too few measurements below $\nu_{\rm pk}$ to allow an independent constraint. A second break is weakly constrained in all three SEDs as $\nu_q \sim 18$–20 GHz (an example of the corner plot with posterior distributions of the fit parameters for $\delta t = 190$ days is shown in Figure D1). Due to large uncertainties on ν_q (in particular up to $\sim$40% for the 182 day SED), we also compute a fit without a ν_q break (i.e., Equation (1)) for each SED, which was the model used by A. Horesh et al. (2021a). Comparing the two models, we find that ΔAIC $<$ 2 and ΔBIC $<$ 2, indicating no strong preference for either model (Table C1).

Table C1
Values of AIC and BIC for the Different Models at Various Epochs

δt[a]	0 Break		1 Break		2 Breaks	
(days)	AIC	BIC	AIC	BIC	AIC	BIC
182	⋯	⋯	17.0	16.4	15.9	15.1
190	⋯	⋯	23.3	25.2	22.5	24.9
197	⋯	⋯	32.8	35.4	30.8	33.9
233[a]	17.4	18.4	14.9	16.3	16.8	18.7
283[a]	18.2	18.3	12.0	12.2	14.6	14.9
1741	40	40.2	34.7	35.0	13.2	13.5
2129	⋯	⋯	10.3	12.4	13.4	15.5
2660	⋯	⋯	53.2	55.5	16.3	11.0
2970	⋯	⋯	25.6	27.5	16.1	18.7

Notes. The three models compared are: (i) a model with 0 breaks represented by $F \propto \nu^{-\alpha_{\rm thin}}$, (ii) a model with 1 break represented by Equation (1), and (iii) a model with 2 breaks represented by Equation (2).

[a] In these SEDs, the "1 Break" model given by Equation (1) has $\nu_{b_1} = \nu_q$, $\alpha_i = \alpha_{\rm thin}$ and $\alpha_j = \alpha_q$.

The SEDs at $\delta t = 233$ days and 283 days do not show strong evidence of a low-frequency turnover (i.e., no $\alpha > 0$ segment is present), but do exhibit a slight steepening at higher frequencies. We fit these SEDs with Equation (1) (with $\nu_{b_1} = \nu_q$, $\alpha_i = \alpha_{\rm thin}$ and $\alpha_j = \alpha_q$), and ν_q is constrained to $\sim$10 GHz in both SEDs. We also attempted a single power-law fit of the form $F \propto \nu^{\alpha_{\rm thin}}$. Based on the AIC and BIC values (given in Table C1) for the two models, the model with *one* break is marginally preferred over a single power law for $\delta t = 233$ days SED (with ΔAIC $= 2.5$ and ΔBIC $= 2.1$) and is strongly preferred for $\delta t = 283$ days (with ΔAIC $= 6.2$ and ΔBIC $= 6.1$). At $\delta t = 369$ days and $\delta t = 576$ days, the SEDs show no low-frequency turnovers or high-frequency steepening, and are therefore fitted with a single power law of the form $F \propto \nu^{\alpha_{\rm thin}}$.

C.2. Fit of SEDs Associated with the Second Radio Flare

We treat the SEDs taken during the second flare (i.e., at $\delta t \gtrsim 1400$ days) independently of the earlier ones, where we let $\alpha_{\rm thick}$ vary freely. Here, instead we try fitting the SEDs with both Equations (2) (with $\alpha_{\rm thick,thin}$ spectral segments) and (1) with $\alpha_{\rm thick} = 5/2$ (as expected for standard self-absorbed synchrotron spectra in the context of TDEs; e.g., K. D. Alexander et al. 2020). Similar to the previous SEDs, we adopt $s_1 = -0.03$ and $s_2 = -0.003$ (unless otherwise mentioned); and the AIC and BIC values are reported in Table C1.

For the SEDs at $\delta t = 1741$ days, 2660 days, and 2970 days, we find that the model with *two* breaks is a better fit. Here, ν_q is constrained to $\sim$7 GHz, $\sim$19 GHz, and $\sim$5 GHz, respectively. In these SEDs, the peak's location largely mirrors the priors, and in particular, the lower bound on the peak frequency remains unconstrained, resulting in only limits on the SED peak. In contrast, the SED at $\delta t = 2129$ days prefers the model with only *one* break, and the peak is robustly constrained. However, this SED exhibits a smoother turnover compared to others, requiring $|s_1| > 0.03$. We thus assume $s_1 = -1$ here and report the results accordingly.

C.3. Model Selection Criteria

We use the Akaike information criterion (AIC) and the Bayesian information criterion (BIC) in Section 3.1 as a means for model selection. These statistical measures compare how well the models fit the observed data, with both criteria penalizing the models that have more parameters. BIC imposes a stricter penalty, making it more conservative. The aim is to achieve an optimal balance between goodness of fit and the complexity of the model.

The AIC is given by:

$$\mathrm{AIC} = 2k - 2\ln(L), \tag{C1}$$

and the BIC is given by:

$$\mathrm{BIC} = k\ln(n) - 2\ln(L) \tag{C2}$$

where k is the number of free parameters used in our MCMC fitting, L is the maximum likelihood of the model, and n is the number of observations.

As mentioned in Section 3.1, we use one or more models to fit for some SEDs. The models are as follows: (i) models with 0 breaks are represented by $F \propto \nu^{\alpha_{\rm thin}}$, (ii) models with 1 break are given by Equation (1), and (iii) models with 2 breaks are given by Equation (2). We give the corresponding AIC and BIC in Table C1. Values of ΔAIC > 2 and ΔBIC > 2 show a statistically stronger preference for the model with the *lower* AIC and BIC values.

Appendix D
Posterior Distribution of Fit Parameters of the Radio SED at $\delta t = 190$ days

We use the model "Equation (1) × Equation (2)" to fit the SEDs at $\delta t = 182$–197 days. The following priors were used: $0 < F_{\rm pk} < 40$ mJy; $0 < \nu_{\rm pk} < 40$ GHz; $-3 < \alpha_{\rm thin} < 0$; $0 < \alpha_{\rm thick} < 3$; and $\nu_{\rm pk} < \nu_q < 40$ GHz. All priors have a uniform distribution. As an example, we present the posterior distributions of $F_{\rm pk}$, $\nu_{\rm pk}$, $\alpha_{\rm thin}$, $\alpha_{\rm thick}$, and ν_q resulting from the MCMC fitting of the SED at $\delta t = 190$ days in Figure D1.

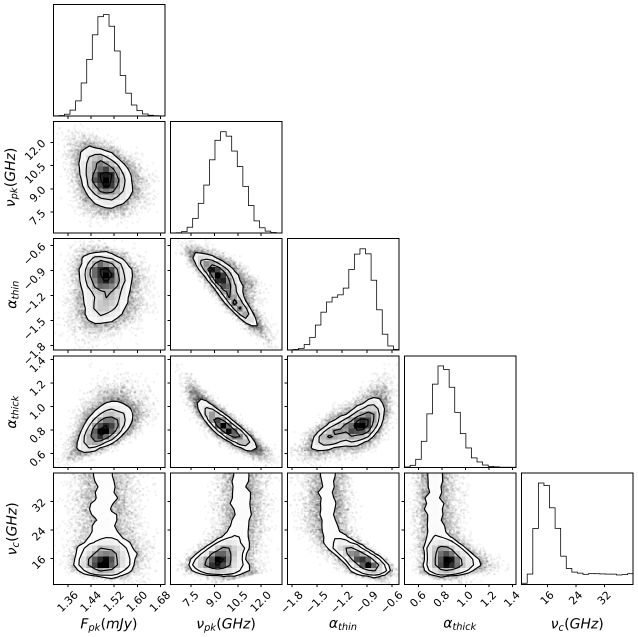

Figure D1. One- and two-dimensional projections of the posterior distributions of the free parameters resulting from the fitting of the radio SED at $\delta t = 190$ days with the model "Equation (1) × Equation (2)". The contours are drawn at the 68%, 95%, and 99% credible levels. As can be seen, all of the parameters are well constrained.

Appendix E
Expressions for Synchrotron Physical Parameters in the Case of $p > 2$

L. DeMarchi et al. (2022) derived the following expressions for the physical parameters in the synchrotron model, assuming $\gamma_{\rm max} \rightarrow \infty$. A key aspect of these equations is, therefore, $p > 2$. In Section 3 and Table 2, we use these equations to measure B, R, U, and $n_{\rm e}$ for the SEDs where $p > 2$,

$$B = (2.50 \times 10^9\ {\rm G})\left(\frac{\nu_{\rm pk}}{5\ {\rm GHz}}\right)\left(\frac{1}{c_1}\right) \times \left[4.69 \times 10^{-23}\left(\frac{E_l}{\rm erg}\right)^{2(2-p)}(\epsilon_B/\epsilon_e)^2 c_5 \sin(\theta)^{\frac{1}{2}(-5-2p)} \times (p-2)^{-2}\left(\frac{D}{\rm Mpc}\right)^{-2}\left(\frac{f}{0.5}\right)^{-2}\left(\frac{F_{\rm pk}}{\rm Jy}\right)^{-1} c_6^{-3}\right]^{\frac{2}{13+2p}} \tag{E1}$$

$$R = (2.50 \times 10^9)^{-1}\ {\rm cm} \times c_1\left(\frac{\nu_{\rm pk}}{5\ {\rm GHz}}\right)^{-1} \times [12\epsilon_B c_5^{-(6+p)} c_6^{(5+p)}(9.52 \times 10^{25})^{(6+p)}\sin^2\theta \times \pi^{-(5+p)}\left(\frac{D}{\rm Mpc}\right)^{2(6+p)}\left(\frac{E_l}{\rm erg}\right)^{(2-p)}\left(\frac{F_{\rm pk}}{\rm Jy}\right)^{(6+p)} \times \left(\epsilon_e(p-2)\left(\frac{f}{0.5}\right)\right)^{-1}\Bigg]^{1/(13+2p)} \tag{E2}$$

$$U = c_1(3.33 \times 10^{-11}\ {\rm erg})\,\epsilon_B^{-1}10^{\frac{75(6+p)}{13+2p}}\left(\frac{f}{0.5}\right)\left(\frac{\nu_{\rm pk}}{5\ {\rm GHz}}\right)^{-1} \times \left[3.086^{6(6+p)}4.411 \times 10^{-96}\left(\frac{D}{\rm Mpc}\right)^{28+6p} \times \left(\frac{F_{\rm pk}}{\rm Jy}\right)^{14+3p}\pi^{-3(1+p)}\sin\theta^{-4(1+p)}c_5^{-(14+3p)}c_6^{3(1+p)} \times \left(2\epsilon_B\epsilon_e^{-1}(p-2)^{-1}\left(\frac{E_l}{\rm erg}\right)^{2-p} \times \left(\frac{f}{0.5}\right)^{-1}\right)^{11}\right]^{1/(13+2p)} \tag{E3}$$

$$n_{\rm e} = \left(\frac{i+2}{2\epsilon_{\rm B}}\right)\left(\frac{B^2}{8\pi}\right)(\mu_e m_p)^{-1}(qv)^{-2} \tag{E4}$$

where f is a volume filling factor that represents the fraction of a sphere of radius R that is emitting synchrotron radiation; c_1, $c_5(p)$, and $c_6(p)$ are synchrotron coefficients (see, e.g., L. DeMarchi et al. 2022); and D is the distance of the TDE in megaparsecs. E_l is the lowest energy of the electrons accelerated to the power law. They constitute the electrons with the minimum Lorentz factor $\gamma_{\rm min}$. θ is the angle between the electron velocity vector and the B field. In Equation (E4), i is the adiabatic index of the shocked gas, $\mu_{\rm e}$ is the mean molecular weight per electron, $m_{\rm p}$ is the mass of the proton, and q is the power-law index of expansion of the radius with time (i.e., $R \propto t^q$). We adopt $f = 0.5$, $\sin(\theta) \approx 1$ and $\gamma_{\rm min} = 1$, which gives $E_l = m_e c^2$, $i = 1$, and lastly, $q = 0.88$. This value of q follows from an assumption of the contrast in the power law of the ambient density the shock is expanding into, and the power law of the density of the ejecta.

Appendix F
Derivation of Synchrotron Physical Parameters in the Case of $p < 2$

In this Section, we derive equations for the physical parameters where $\gamma_{\rm max}$ has a finite upper bound, and is therefore valid for $p < 2$.

The number density distribution of electrons is given by $dN(\gamma_e)/d\gamma_e = K_0\gamma_e^{-p}$ for $\gamma_e \geqslant \gamma_{\rm min}$, where N is the number of electrons per unit volume, K_0 is the normalization constant, p is the power-law index of the electron population distribution. Number density distribution of electrons can also be expressed as $dN/dE = N_0E^{-p}$ in energy space, where N_0 is the normalization constant, and $E = \gamma_e m_e c^2$. This gives $K_0\gamma_e^{-p}d\gamma_e = N_0E^{-p}dE \Rightarrow K_0(m_ec^2)^{p-1} = N_0$.

The relativistic electron energy density is given by:

$$\begin{aligned} E_\mathrm{e} &= \int_{E_l}^{E_u} E N_0 E^{-p} dE \\ &= \int_{\gamma_\mathrm{min}}^{\gamma_\mathrm{max}} (\gamma_e m_e c^2) K_0 \gamma_e^{-p} d\gamma_e \\ &= K_0 m_e c^2 \left[\frac{\gamma_e^{2-p}}{2-p}\right]\Big|_{\gamma_\mathrm{min}}^{\gamma_\mathrm{max}}. \end{aligned} \tag{F1}$$

If $\gamma_\mathrm{max} \rightarrow \infty$, Equation (F1) will revert to the form used for deriving Equations (E1)–(E4) and will require $p > 2$ to be finite. However, if we impose a finite γ_max, then, the new E_e will take the following form:

$$\begin{aligned} E_\mathrm{e} &= \frac{K_0 m_e c^2 \gamma_\mathrm{min}^{2-p}}{2-p}\left[\left(\frac{\gamma_\mathrm{max}}{\gamma_\mathrm{min}}\right)^{2-p} - 1\right] \\ &= \frac{K_0 (m_e c^2)^{p-1} E_l^{2-p}}{2-p}\Lambda \\ &= \frac{N_0 E_l^{2-p}}{2-p}\Lambda \end{aligned} \tag{F2}$$

for $p < 2$, where $\Lambda = [(\gamma_\mathrm{max}/\gamma_\mathrm{min})^{2-p} - 1]$, and $E_l = \gamma_\mathrm{min} m_e c^2$, and $p < 2$ is valid. Using this new expression of E_e, we follow L. DeMarchi et al. (2022) to derive B, R, and U as follows:

$$\begin{aligned} B = (2.50 \times 10^9\ \mathrm{G})&\left(\frac{\nu_\mathrm{pk}}{5\ \mathrm{GHz}}\right)\left(\frac{1}{c_1}\right) \\ &\times [4.69 \times 10^{-23}\left(\frac{E_l}{\mathrm{erg}}\right)^{2(2-p)}\Lambda^2\left(\frac{\epsilon_B}{\epsilon_e}\right)^2 c_5 \sin(\theta)^{\frac{1}{2}(-5-2p)} \\ &\times (2-p)^{-2}\left(\frac{D}{\mathrm{Mpc}}\right)^{-2}\left(\frac{f}{0.5}\right)^{-2}\left(\frac{F_\mathrm{pk}}{\mathrm{Jy}}\right)^{-1} c_6^{-3}]^{\frac{2}{13+2p}} \end{aligned} \tag{F3}$$

$$\begin{aligned} R = (2.50 \times 10^9)^{-1}\ \mathrm{cm} \times c_1&\left(\frac{\nu_\mathrm{pk}}{5\mathrm{GHz}}\right)^{-1} \\ &\times [12\epsilon_B c_5^{-(6+p)} c_6^{(5+p)} (9.52 \times 10^{25})^{(6+p)} \sin^2\theta \\ &\times \pi^{-(5+p)}\left(\frac{D}{\mathrm{Mpc}}\right)^{2(6+p)}\left(\frac{E_l}{\mathrm{erg}}\right)^{(2-p)}\Lambda\left(\frac{F_\mathrm{pk}}{\mathrm{Jy}}\right)^{(6+p)} \\ &\times \left(\epsilon_e(2-p)\left(\frac{f}{0.5}\right)\right)^{-1}\Bigg]^{1/(13+2p)} \end{aligned} \tag{F4}$$

$$\begin{aligned} U = c_1(3.33 \times 10^{-11}\ \mathrm{erg})\,\epsilon_B^{-1} 10^{\frac{75(6+p)}{13+2p}}&\left(\frac{f}{0.5}\right)\left(\frac{\nu_\mathrm{pk}}{5\mathrm{GHz}}\right)^{-1} \\ &\times \Bigg[3.086^{6(6+p)} 4.411 \times 10^{-96}\left(\frac{D}{\mathrm{Mpc}}\right)^{28+6p} \\ &\times \left(\frac{F_\mathrm{pk}}{\mathrm{Jy}}\right)^{14+3p}\pi^{-3(1+p)}\sin\theta^{-4(1+p)} c_5^{-(14+3p)} c_6^{3(1+p)} \\ &\times\left(2\epsilon_B \epsilon_e^{-1}(2-p)^{-1}\left(\frac{E_l}{\mathrm{erg}}\right)^{2-p}\Lambda\left(\frac{f}{0.5}\right)^{-1}\right)^{11}\Bigg]^{1/(13+2p)} \end{aligned} \tag{F5}$$

Appendix G
Host SMBH Mass Estimates for ASASSN-15oi

There have been a wide range of host SMBH mass estimates in the literature: $1.3 \times 10^7\, M_\odot$ (T. W. S. Holoien et al. 2016; using the galactic scaling relationship between M_bulge and M_BH); $0.5^{+1.4}_{-0.4} \times 10^6\, M_\odot$ (T. Wevers et al. 2019, 2020; using M_BH–σ relationship in L. Ferrarese & H. Ford 2005); $(4 \pm 1) \times 10^6\, M_\odot$ (B. Mockler et al. 2019); $(5.4 \pm 4.6) \times 10^6\, M_\odot$ (S. Wen et al. 2020; using their slim-disk model); $9 \times 10^6\, M_\odot$ (A. Mummery 2021; using their evolving relativistic accretion disk model fit to the existing X-ray observations); $4.7^{+15}_{-3.4} \times 10^6\, M_\odot$ (A. Mummery et al. 2023; derived with their mean X-ray radius–M_BH relation), and $7^{+5}_{-5} \times 10^5\, M_\odot$ (A. Mummery et al. 2024; using their scaling relationships between late-time UV plateau luminosity and M_BH). Here, we adopt $2.5 \times 10^6\, M_\odot$ as the SMBH mass, following S. Gezari et al. (2017).

ORCID iDs

A. Hajela https://orcid.org/0000-0003-2349-101X
R. Margutti https://orcid.org/0000-0003-4768-7586
R. Chornock https://orcid.org/0000-0002-7706-5668
C. T. Christy https://orcid.org/0000-0003-0528-202X
M. Stroh https://orcid.org/0000-0002-3019-4577
G. Terreran https://orcid.org/0000-0003-0794-5982
S. Komossa https://orcid.org/0000-0003-4183-4215
J. S. Bright https://orcid.org/0000-0002-7735-5796
E. Ramirez-Ruiz https://orcid.org/0000-0003-2558-3102
D. L. Coppejans https://orcid.org/0000-0001-5126-6237
J. K. Leung https://orcid.org/0000-0002-9415-3766
T. Laskar https://orcid.org/0000-0003-1792-2338
A. Horesh https://orcid.org/0000-0002-5936-1156
G. Schroeder https://orcid.org/0000-0001-9915-8147
Nayana A. J. https://orcid.org/0000-0002-8070-5400
M. H. Wieringa https://orcid.org/0000-0002-7721-8660
S. Gomez https://orcid.org/0000-0001-6395-6702
M. Nicholl https://orcid.org/0000-0002-2555-3192
H. Sears https://orcid.org/0000-0001-8023-4912
B. A. Zauderer https://orcid.org/0000-0003-1152-518X

References

Alexander, K. D., Berger, E., Guillochon, J., Zauderer, B. A., & Williams, P. K. G. 2016, ApJL, 819, L25
Alexander, K. D., van Velzen, S., Horesh, A., & Zauderer, B. A. 2020, SSRv, 216, 81
Anderson, M. M., Mooley, K. P., Hallinan, G., et al. 2020, ApJ, 903, 116
Andreoni, I., Coughlin, M. W., Perley, D. A., et al. 2022, Natur, 612, 430
Anumarlapudi, A., Dobie, D., Kaplan, D. L., et al. 2024, ApJ, 974, 241
Assef, R. J., Stern, D., Kochanek, C. S., et al. 2013, ApJ, 772, 26
Assef, R. J., Stern, D., Noirot, G., et al. 2018, ApJS, 234, 23
Auchettl, K., Guillochon, J., & Ramirez-Ruiz, E. 2017, ApJ, 838, 149
Barniol Duran, R., Nakar, E., & Piran, T. 2013, ApJ, 772, 78
Berger, E., Zauderer, A., Pooley, G. G., et al. 2012, ApJ, 748, 36
Bietenholz, M., Bartel, N., Rupen, M. P., et al. 2010, in Proc. of the 10th European VLBI Network Symp. and EVN Users Meeting: VLBI and the New Generation of Radio Arrays (Trieste: SISSA), 57
Björnsson, C. I., & Keshavarzi, S. T. 2017, ApJ, 841, 12
Bloom, J. S., Giannios, D., Metzger, B. D., et al. 2011, Sci, 333, 203
Bonnerot, C., & Stone, N. C. 2021, SSRv, 217, 16
Breeveld, A. A., Curran, P. A., Hoversten, E. A., et al. 2010, MNRAS, 406, 1687
Brimacombe, J., Brown, J. S., Holoien, T. W. S., et al. 2015, ATel, 7910, 1
Brown, G. C., Levan, A. J., Stanway, E. R., et al. 2015, MNRAS, 452, 4297
Brown, G. C., Levan, A. J., Stanway, E. R., et al. 2017, MNRAS, 472, 4469
Brown, P. J., Holland, S. T., Immler, S., et al. 2009, AJ, 137, 4517
Burrows, D. N., Hill, J. E., Nousek, J. A., et al. 2005, SSRv, 120, 165
Burrows, D. N., Kennea, J. A., Ghisellini, G., et al. 2011, Natur, 476, 421
Cannizzaro, G., Wevers, T., Jonker, P. G., et al. 2021, MNRAS, 504, 792
Cannizzo, J. K., Lee, H. M., & Goodman, J. 1990, ApJ, 351, 38
Cardelli, J. A., Clayton, G. C., & Mathis, J. S. 1989, ApJ, 345, 245
Cendes, Y., Alexander, K. D., Berger, E., et al. 2021a, ApJ, 919, 127
Cendes, Y., Berger, E., Alexander, K. D., et al. 2022, ApJ, 938, 28
Cendes, Y., Berger, E., Alexander, K. D., et al. 2024, ApJ, 971, 185

Cendes, Y., Eftekhari, T., Berger, E., & Polisensky, E. 2021b, ApJ, 908, 125
Cenko, S. B., Krimm, H. A., Horesh, A., et al. 2012, ApJ, 753, 77
Charalampopoulos, P., Leloudas, G., Malesani, D. B., et al. 2022, A&A, 659, A34
Chevalier, R. A. 1998, ApJ, 499, 810
Chevalier, R. A., & Fransson, C. 2017, in Handbook of Supernovae, ed. A. W. Alsabti & P. Murdin (Cham: Springer), 875
Christy, C. T., Alexander, K. D., Cendes, Y., et al. 2024, ApJ, 974, 18
Clark, B. G. 1980, A&A, 89, 377
Czerny, B., Różańska, A., Janiuk, A., & Życki, P. T. 2000, NewAR, 44, 439
Dai, J. L., Lodato, G., & Cheng, R. 2021, SSRv, 217, 12
Dai, L., McKinney, J. C., Roth, N., Ramirez-Ruiz, E., & Miller, M. C. 2018, ApJL, 859, L20
De Colle, F., Guillochon, J., Naiman, J., & Ramirez-Ruiz, E. 2012, ApJ, 760, 103
DeMarchi, L., Margutti, R., Dittman, J., et al. 2022, ApJ, 938, 84
Done, C., Gierliński, M., & Kubota, A. 2007, A&ARv, 15, 1
Eftekhari, T., Berger, E., Zauderer, B. A., Margutti, R., & Alexander, K. D. 2018, ApJ, 854, 86
Esin, A. A., McClintock, J. E., & Narayan, R. 1997, ApJ, 489, 865
Evans, C. R., & Kochanek, C. S. 1989, ApJL, 346, L13
Evans, P. A., Beardmore, A. P., Page, K. L., et al. 2009, MNRAS, 397, 1177
Ferrarese, L., & Ford, H. 2005, SSRv, 116, 523
Fitzpatrick, E. L. 1999, PASP, 111, 63
Foreman-Mackey, D., Hogg, D. W., Lang, D., & Goodman, J. 2013, PASP, 125, 306
Gehrels, N., Chincarini, G., Giommi, P., et al. 2004, ApJ, 611, 1005
Gezari, S. 2021, ARA&A, 59, 21
Gezari, S., Cenko, S. B., & Arcavi, I. 2017, ApJL, 851, L47
Goodwin, A. J., Alexander, K. D., Miller-Jones, J. C. A., et al. 2023, MNRAS, 522, 5084
Goodwin, A. J., Mummery, A., Laskar, T., et al. 2025, ApJ, 981, 122
Goodwin, A. J., van Velzen, S., Miller-Jones, J. C. A., et al. 2022, MNRAS, 511, 5328
Greisen, E. W. 2003, in Astrophysics and Space Science Library, Vol. 285, Information Handling in Astronomy—Historical Vistas, ed. A. Heck (Dordrecht: Kluwer), 109
Guillochon, J., Manukian, H., & Ramirez-Ruiz, E. 2014, ApJ, 783, 23
Guillochon, J., & Ramirez-Ruiz, E. 2013, ApJ, 767, 25
Guolo, M., Gezari, S., Yao, Y., et al. 2024, ApJ, 966, 160
Hammerstein, E., van Velzen, S., Gezari, S., et al. 2023, ApJ, 942, 9
Hills, J. G. 1975, Natur, 254, 295
Hinkle, J. T., Holoien, T. W. S., Shappee, B. J., & Auchettl, K. 2021, ApJ, 910, 83
Högbom, J. A. 1974, A&AS, 15, 417
Holoien, T. W. S., Brown, J. S., Auchettl, K., et al. 2018, MNRAS, 480, 5689
Holoien, T. W. S., Kochanek, C. S., Prieto, J. L., et al. 2016, MNRAS, 463, 3813
Horesh, A., Cenko, S. B., & Arcavi, I. 2021a, NatAs, 5, 491
Horesh, A., Sfaradi, I., Fender, R., et al. 2021b, ApJL, 920, L5
Jansen, F., Lumb, D., Altieri, B., et al. 2001, A&A, 365, L1
Kalberla, P. M. W., Burton, W. B., Hartmann, D., et al. 2005, A&A, 440, 775
Kellermann, K. I., & Pauliny-Toth, I. I. K. 1969, ApJL, 155, L71
Komossa, S. 2002, RvMA, 15, 27
Komossa, S., & Grupe, D. 2023, AN, 344, e20230015
Krolik, J., Piran, T., Svirski, G., & Cheng, R. M. 2016, ApJ, 827, 127
Lacy, M., Baum, S. A., Chandler, C. J., et al. 2020, PASP, 132, 035001
Levan, A. J., Tanvir, N. R., Cenko, S. B., et al. 2011, Sci, 333, 199
Loeb, A., & Ulmer, A. 1997, ApJ, 489, 573
Lu, W., & Bonnerot, C. 2020, MNRAS, 492, 686
Lu, W., & Kumar, P. 2018, ApJ, 865, 128
Margutti, R., Zaninoni, E., Bernardini, M. G., et al. 2013, MNRAS, 428, 729
Matsumoto, T., & Piran, T. 2023, MNRAS, 522, 4565
Metzger, B. D. 2022, ApJL, 937, L12
Metzger, B. D., & Stone, N. C. 2016, MNRAS, 461, 948
Mezger, P. G., & Henderson, A. P. 1967, ApJ, 147, 471
Miller, M. C. 2015, ApJ, 805, 83
Mockler, B., Guillochon, J., & Ramirez-Ruiz, E. 2019, ApJ, 872, 151
Mockler, B., & Ramirez-Ruiz, E. 2021, ApJ, 906, 101
Mou, G., Dou, L., Jiang, N., et al. 2021, ApJ, 908, 197
Mummery, A. 2021, arXiv:2104.06212
Mummery, A., & Balbus, S. A. 2020, MNRAS, 492, 5655
Mummery, A., van Velzen, S., Nathan, E., et al. 2024, MNRAS, 527, 2452
Mummery, A., Wevers, T., Saxton, R., & Pasham, D. 2023, MNRAS, 519, 5828
Narayan, R., & Yi, I. 1994, ApJL, 428, L13
Nicholl, M., Pasham, D. R., Mummery, A., et al. 2024, Natur, 634, 804
Park, J., Caprioli, D., & Spitkovsky, A. 2015, PhRvL, 114, 085003
Perlman, E. S., Meyer, E. T., Wang, Q. D., et al. 2022, ApJ, 925, 143
Piran, T., Svirski, G., Krolik, J., Cheng, R. M., & Shiokawa, H. 2015, ApJ, 806, 164
Poole, T. S., Breeveld, A. A., Page, M. J., et al. 2008, MNRAS, 383, 627
Rees, M. J. 1988, Natur, 333, 523
Roming, P. W. A., Kennedy, T. E., Mason, K. O., et al. 2005, SSRv, 120, 95
Roth, N., Kasen, D., Guillochon, J., & Ramirez-Ruiz, E. 2016, ApJ, 827, 3
Sato, Y., Murase, K., Bhattacharya, M., et al. 2024, PhRvD, 110, L061307
Sault, R. J., Teuben, P. J., & Wright, M. C. H. 1995, in ASP Conf. Ser. 77, Astronomical Data Analysis Software and Systems IV, ed. R. A. Shaw, H. E. Payne, & J. J. E. Hayes (San Francisco, CA: ASP), 433
Sault, R. J., & Wieringa, M. H. 1994, A&AS, 108, 585
Saxton, R., Komossa, S., Auchettl, K., & Jonker, P. G. 2021, SSRv, 217, 18
Schlafly, E. F., & Finkbeiner, D. P. 2011, ApJ, 737, 103
Sfaradi, I., Beniamini, P., Horesh, A., et al. 2024, MNRAS, 527, 7672
Sfaradi, I., Horesh, A., Fender, R., et al. 2022, ApJ, 933, 176
Shappee, B., Prieto, J., Stanek, K. Z., et al. 2014, AAS Meeting, 223, 236.03
Shen, R. F., & Matzner, C. D. 2014, ApJ, 784, 87
Sironi, L., Spitkovsky, A., & Arons, J. 2013, ApJ, 771, 54
Sniegowska, M., Czerny, B., Bon, E., & Bon, N. 2020, A&A, 641, A167
Steinberg, E., & Stone, N. C. 2024, Natur, 625, 463
Thomsen, L. L., Kwan, T. M., Dai, L., et al. 2022, ApJL, 937, L28
Tingay, S. J., Jauncey, D. L., King, E. A., et al. 2003, PASJ, 55, 351
van der Klis, M. 2004, arXiv:astro-ph/0410551
van Velzen, S., Anderson, G. E., Stone, N. C., et al. 2016, Sci, 351, 62
van Velzen, S., Stone, N. C., Metzger, B. D., et al. 2019, ApJ, 878, 82
Veronese, S., Vignali, C., Severgnini, P., Matzeu, G. A., & Cignoni, M. 2024, A&A, 683, A131
Weiler, K. W., Panagia, N., Montes, M. J., & Sramek, R. A. 2002, ARA&A, 40, 387
Wen, S., Jonker, P. G., Stone, N. C., Zabludoff, A. I., & Psaltis, D. 2020, ApJ, 897, 80
Wevers, T., Pasham, D. R., van Velzen, S., et al. 2021, ApJ, 912, 151
Wevers, T., Stone, N. C., van Velzen, S., et al. 2019, MNRAS, 487, 4136
Wevers, T., Stone, N. C., van Velzen, S., et al. 2020, MNRAS, 493, 1498
Wevers, T., van Velzen, S., Jonker, P. G., et al. 2017, MNRAS, 471, 1694
Williams, P. K. G., Clavel, M., Newton, E., & Ryzhkov, D., 2017 pwkit: Astronomical Utilities in Python, Astrophysics Source Code Library, ascl:1704.001
Wilson, W. E., Ferris, R. H., Axtens, P., et al. 2011, MNRAS, 416, 832
Wright, E. L., Eisenhardt, P. R. M., Mainzer, A. K., et al. 2010, AJ, 140, 1868
Yao, Y., Lu, W., Guolo, M., et al. 2022, ApJ, 937, 8
Yao, Y., Ravi, V., Gezari, S., et al. 2023, ApJL, 955, L6
Zauderer, B. A., Berger, E., Margutti, R., et al. 2013, ApJ, 767, 152
Zauderer, B. A., Berger, E., Soderberg, A. M., et al. 2011, Natur, 476, 425
Zhuang, J., Shen, R.-F., Mou, G., & Lu, W. 2025, ApJ, 979, 109